Bulletin of Mathematical Biology (2024) 86:134
https://doi.org/10.1007/s11538-024-01360-7

Society for Mathematical Biology

ORIGINAL ARTICLE

Modelling Mucus Clearance in Sinuses: Thin-Film Flow Inside a Fluid-Producing Cavity Lined with an Active Surface

Nikhil Desai [1] · **Eric Lauga** [1]

Received: 6 June 2024 / Accepted: 16 September 2024 / Published online: 5 October 2024

Abstract

The paranasal sinuses are a group of hollow spaces within the human skull, surrounding the nose. They are lined with an epithelium that contains mucus-producing cells and tiny hairlike active appendages called cilia. The cilia beat constantly to sweep mucus out of the sinus into the nasal cavity, thus maintaining a clean mucus layer within the sinuses. This process, called mucociliary clearance, is essential for a healthy nasal environment and disruption in mucus clearance leads to diseases such as chronic rhinosinusitis, specifically in the maxillary sinuses, which are the largest of the paranasal sinuses. We present here a continuum mathematical model of mucociliary clearance inside the human maxillary sinus. Using a combination of analysis and computations, we study the flow of a thin fluid film inside a fluid-producing cavity lined with an active surface: fluid is continuously produced by a wall-normal flux in the cavity and then is swept out, against gravity, due to an effective tangential flow induced by the cilia. We show that a steady layer of mucus develops over the cavity surface only when the rate of ciliary clearance exceeds a threshold, which itself depends on the rate of mucus production. We then use a scaling analysis, which highlights the competition between gravitational retention and cilia-driven drainage of mucus, to rationalise our computational results. We discuss the biological relevance of our findings, noting that measurements of mucus production and clearance rates in healthy sinuses fall within our predicted regime of steady-state mucus layer development.

Keywords Mucus transport · Sinuses · Fluid mechanics · Thin films · Active flows · Lubrication

1 Introduction

The human skull contains air-filled cavities around the nose region, called paranasal sinuses. These are named after the bones in the skull within which they reside:

✉ Eric Lauga
e.lauga@damtp.cam.ac.uk

[1] Department of Applied Mathematics and Theoretical Physics, University of Cambridge, Cambridge CB3 0WA, UK

frontal, maxillary, ethmoid and sphenoid (Papadopoulou et al. 2021) (see illustration in Fig. 1a). The sinuses are believed to serve a number of evolutionary and functional purposes, including keeping the skull light and buoyant, imparting resonance to voice, humidifying inspired air, improving olfaction, absorbing physical trauma and producing mucus (Blanton and Biggs 1969; Keir 2008).

One role of sinuses is to supply mucus to the nasal cavity, where it plays an important role in the respiratory system (Cohen 2006). The sinus interior is lined with an epithelium which contains two types of cells: (i) goblet cells that secrete gel-forming proteins called mucin, and, (ii) ciliated cells endowed with active hairlike appendages called cilia (Fahy and Dickey 2010). The epithelium is hydrated through osmosis regulated by ion transport across the epithelial cells (Hill et al. 2022). The secreted mucins expand drastically upon contacting the hydrated epithelium and form a gel-like fluid called mucus (McShane et al. 2021). In this way, mucus is effectively produced inside the sinuses through a combination of mucin-secretion by goblet cells and osmosis-induced hydration of the epithelium. The typical composition of mucus is: $\approx 97.5\%$ water, $\approx 0.5\%$ mucin proteins, $\approx 1.1\%$ each of salts and $\approx 0.9\%$ other globular proteins (Hill et al. 2022). It is a bi-layered viscoelastic fluid consisting of a highly viscous mucus layer (ML) overlying a periciliary layer (PCL) which itself rests atop the nasal epithelium (Kaliner et al. 1984; Knowles and Boucher 2002). The PCL has been classically postulated to be a water-like fluid layer, but more recent investigations have questioned this gel-on-liquid description, instead proposing that the PCL has a brush-like structure owing to various secreted mucins and other polymers adhered to the epithelium (Button et al. 2012). Regardless, the cilia are immersed almost entirely in the PCL with only their tips penetrating into the ML (Sanderson and Sleigh 1981; Satir and Sleigh 1990) (see Fig. 1b). They perform coordinated motion in a forward and recovery stroke such that they push the mucus during the forward stroke but cause minimal backflow during the recovery stroke; thus, on average, the mucus blanket is transported along the sinus epithelium (Proctor and Andersen 1982; Satir and Sleigh 1990). The net effect of cilia-induced mucus transport is that the mucus exits the sinus through an opening called the ostium, and is then directed into the nasopharynx (Beule 2010) (see Fig. 1c). In this way, a fresh mucus layer is always maintained inside a healthy sinus: being produced continuously at the epithelium, and being cleared out simultaneously by the beating cilia. This process, of constant production and replenishment of mucus, is referred to as mucociliary clearance (MCC) (Jones 2001).

MCC is a robust process that is responsible for health and defence of the nose, for example, almost all of the particulate matter of size $> 10\ \mu$m that we breathe gets trapped in the mucus and removed before it can cause harm to the underlying tissue (Cohen 2006). Importantly, inhaled bacteria are removed by MCC before they get time to replicate and become infectious. Any impairment in MCC can cause mucus build-up inside the sinuses; situations causing excess mucus production (e.g., allergen-induced inflammation of the sinonasal mucosa) can impair MCC and lead to further mucus build-up in the sinuses. These malfunctions are conducive for bacteria to colonise the sinuses, leading to the development of bacterial biofilms and subsequent diseases such as chronic rhinosinusitis (Stevens et al. 2015). It is therefore crucial to understand the physical factors affecting mucus flow in the sinuses, particularly in the maxillary sinus, which is the main site for sinus disease (Fokkens et al. 2020).

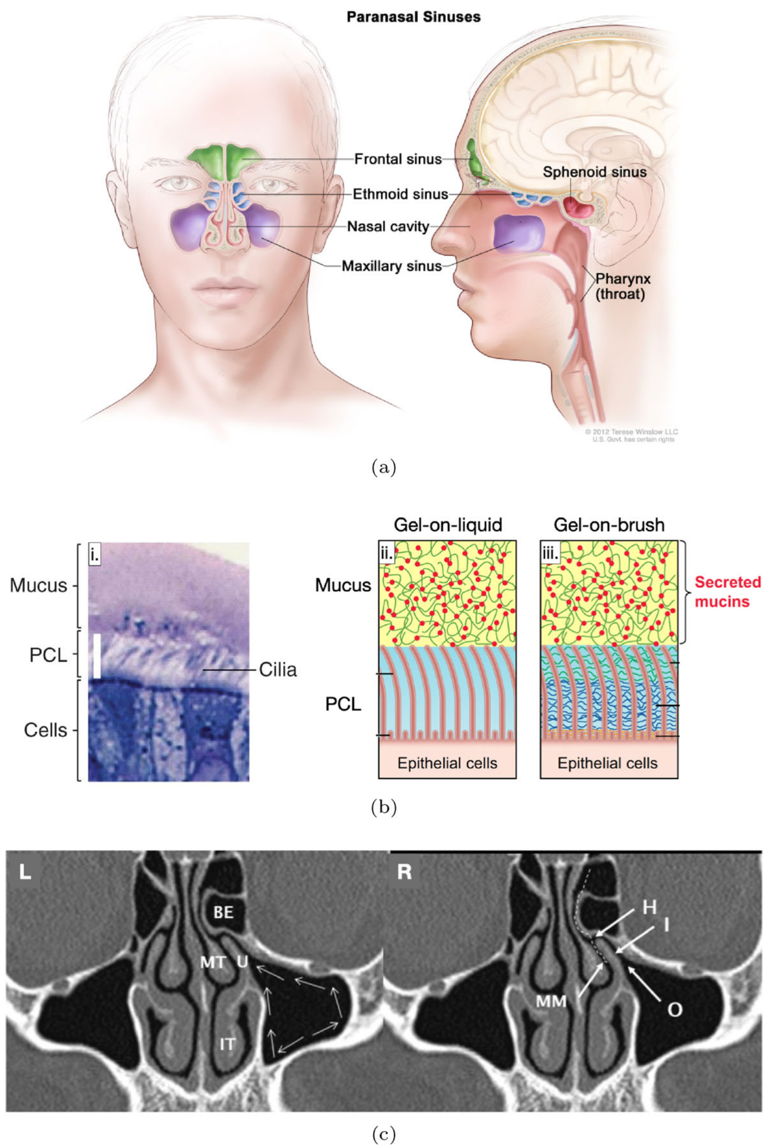

Fig. 1 Mucociliary clearance in human sinuses. **a** Sketch of sinuses and their locations inside the human skull (Winslow 2012). **b**i Light microscopy image of the nasal epithelium, showing goblet cells, cilia, the periciliary layer (PCL) and the mucus layer (ML) (reproduced with permission from Button et al. (2012)). **b**ii Sketch showing the position of the cilia tips and the interface between the PCL and the ML, for the gel-on-liquid model. **b**iii Sketch showing the interface between the PCL and the ML, for the gel-on-brush model (reproduced with permission from Hill et al. (2022)). **c** The maxillary sinuses as seen on a CT scan of a human head. The expected direction of mucus flow due to ciliary beating is shown via the thin white arrows in the left (**L**) sub-panel. The sinus exit, called the ostium, is marked by the letter “O” in the right (**R**) sub-panel (reproduced with permission from Whyte and Boeddinghaus (2019))

A number of interesting fluid flow phenomena govern the evolution and transport of mucus inside the maxillary sinus. Firstly, in order to maintain a steady mucus layer over the sinus walls, there must exist a balance between the rates of mucus production and mucus expulsion due to transport facilitated by ciliated cells. In fact, the thickness of the mucus layer–itself an indicator of susceptibility to disease (Olivença et al. 2019)–would depend on the relative rates of mucus production and mucus clearance. Secondly, since the maxillary sinus ostium is located above the bottom side of the sinus (Whyte and Boeddinghaus 2019), the flowing mucus must overcome gravity in order to successfully exit the sinus (see Fig. 1c). Indeed, it has been clinically postulated that the proclivity of the maxillary sinus to infections is likely due to its ostium being located against the direction of gravity (Bluestone et al. 2012; Butaric et al. 2018; Kim et al. 2021). Thirdly, the mucus layer inside the sinus is exposed to air and can deform due to surface tension, which can then affect its flow.

In this paper, we employ fundamental concepts from fluid mechanics to understand how the aforementioned physical effects interact with each other and contribute to maintain a thin mucus layer inside the maxillary sinus. We first propose in Sect. 2 a model system that includes relevant bio-physical components dictating mucus flow inside the sinus. The system is comprised of a cavity lined with a fluid-producing active surface, i.e. the inner surface of the cavity produces mucus, and also drives it along the cavity with a prescribed tangential velocity which models the mean action of the cilia on the mucus. In Sect. 3, we derive a nonlinear evolution equation for the thickness of the mucus film, based on important modifications to classical theories on thin-film flow (Oron et al. 1997; Craster and Matar 2009; Qin et al. 2020; McKinlay et al. 2023); this is done for both two-dimensional and three-dimensional cavities. In Sect. 4, we solve this equation numerically to study the nature of mucus film profiles inside the model sinus. Specifically, we determine a phase space, defined by the rates of mucus production and clearance, consisting of two types of solutions: unsteady solutions corresponding to physical conditions that do not result in successful MCC, and steady solutions for physical conditions that do result in successful MCC from the sinus. We rationalise this demarcation between the unsteady and steady solutions using a physical argument resulting in a scaling relationship in Sect. 5. We show that, for a prescribed rate of mucus production, successful MCC is achieved only if the cilia-induced mucus flow exceeds a certain threshold; in the process, we identify how this threshold clearance rate scales with the rate of mucus production. In Sect. 6, we next discuss the direct biological application of our findings by comparing our predictions of steady-state conditions in the model sinus (i.e. rates of mucus production and clearance) to the existing literature on these operating conditions in healthy sinuses. We finish by a summary of our work in Sect. 7 along with suggestions for future investigations.

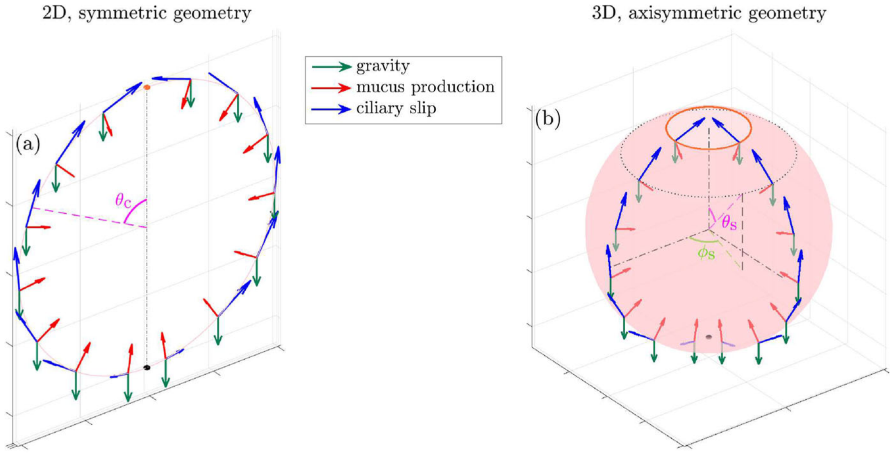

Fig. 2 Schematics explaining the geometry of the model sinus, **a** a two-dimensional, circular system, and, **b** a three-dimensional, but axisymmetric spherical system. The blue arrows denote the direction of the effective ciliary slip velocity $\sim U'_w$, the red arrows denote the wall-normal mucus in-flow V'_w, and the downward pointing green arrows denote the direction of gravity. The bottom-most point in both the cases–from where begins the upward motion of the mucus due to cilia action–is marked by a black dot. The mucus exits the system as soon as it reaches the top: (**a**) the orange dot in the 2D case, and, (**b**) the orange circle in the 3D case. In panel (**b**) the velocity vectors are shown for only two azimuths, for clarity, but they are distributed axisymmetrically–around the vertical axis–over the entire sphere surface

2 Mathematical Model

2.1 Key Biophysical Ingredients

What are the essential ingredients for a minimal model of MCC in the maxillary sinuses? Firstly, it must consist of a finite-size cavity with an outlet for the fluid (mucus) to exit. Biologically, these represent, respectively, the sinus and the ostium (the small opening in the sinus that drains into the nasal cavity). Secondly, there must be some mechanism for fluid production inside the cavity, to model the continuous production of mucus in the sinus. Thirdly, there must also be an active mechanism to continually drive the produced fluid out, modelling the action of the ciliated cells inside the sinus. In healthy conditions, there exists a steady mucus layer in the sinus, which is continuously replenished on account of a balance between mucus production and mucus clearance. This fundamental feature should emerge in our model as a consequence of the forces governing fluid motion.

2.2 The Minimal Model: Simplifying Assumptions

Based on this, we can propose a simple model, which includes all the above-mentioned biophysical effects. For the sinus cavity, we consider two elementary geometries: a circle and a sphere. The former will be used for a planar/two-dimensional analysis whereas the latter for an axisymmetric/three-dimensional analysis. We treat the mucus, in this first exploration, as a Newtonian fluid with uniform physical properties (viscosity and density). We assume that the mucus is continually produced at the walls of the cavity and that it enters the cavity normally (i.e. perpendicular to the local cavity wall) at a constant velocity V'_{w} (red arrows in Fig. 2). Without ciliary function, gravity (green arrows in Fig. 2) would cause the mucus to accumulate inside the cavity and fill it up. But cilia actively sweep the mucus up along the wall and cause it to exit the cavity; the effective action of the cilia is thus modelled as an active (or 'slip') tangential velocity of characteristic magnitude U'_{w}, prescribed along the walls of the cavity (blue arrows in Fig. 2). The mucus exits the system at the top through an ostium which is modelled differently in the two geometries. For the circular geometry, we model the mucus exit as a discontinuity: once the mucus reaches the top-most point (orange dot near the top in Fig. 2a) it is removed from the domain. For the spherical geometry, we truncate the sphere near its top pole to form a small circular opening from where the mucus exits the domain (orange circle near the top in Fig. 2b). We will see that this minimal model is sufficient to explain the development of a thin mucus film inside the sinus (Sect. 6), and will revisit the various assumptions behind the model when offering perspectives for future work (Sect. 7.3).

2.3 Biologically Relevant Parameter Values

We summarise in Table 1 the values of the various important parameters involved in the problem; note that the physical properties of the mucus, especially its effective viscosity and surface tension, can vary over a range of magnitudes, depending on the general health of the nose (Silberberg 1983; Craster and Matar 2000; Smith et al. 2008). In humans, the mucus develops over the sinus epithelium as a film of thickness $h' \sim 10$-$15\ \mu$m (Beule 2010). The coordinated beating of cilia moves this mucus layer at an average rate of 2–25 mm/min (Cohen 2006; Beule 2010; Whyte and Boeddinghaus 2019), which means that U'_{w} lies in the (large) range 30 to 400 μm/s. To estimate typical values of the mucus production rate (V'_{w}) under steady operative conditions, we use a mass balance argument along with measurements of geometrical features of the maxillary sinus. The volume flux coming out of the sinus is

$$Q' \sim h' r'_{\mathrm{o}} U'_{\mathrm{w}} \sim A'_{\mathrm{s}} V'_{\mathrm{w}}, \tag{1}$$

where h' is the height of the mucus film, r'_{o} is the radius of the ostium and A'_{s} is the surface area of the maxillary sinus. The scaling in the first part of Eq. (1) follows from the assumption that in a healthy state, the mucus does not flow out through the total available ostium area (which would be proportional to r'^2_{o}), but only coats the inner surface of the ostium, forming a layer of thickness $\sim h'$. The scaling in the second part of Eq. (1) follows from a mass balance argument that all the mucus secreted from the surface of the sinus must leave through the ostium. Now, if the volume of the sinus is $\mathcal{V}'_{\mathrm{s}}$ and its typical length-scale is ℓ'_{s}, then its internal surface area is,

$$A'_{\mathrm{s}} \sim \mathcal{V}'_{\mathrm{s}} / \ell'_{\mathrm{s}}. \tag{2}$$

Combining Eqs. (1) and (2) yields,

$$V'_\mathrm{w} \sim U'_\mathrm{w} \left(\frac{r'_\mathrm{o} h'}{\mathcal{V}'_\mathrm{s}/\ell'_\mathrm{s}} \right) \sim U'_\mathrm{w} \times \left(O(10^{-6}) - O(10^{-4}) \right). \tag{3}$$

To arrive at the number in brackets in Eq. (3), we have used the following values of the geometric parameters, obtained from measurements on human sinuses: $h' \sim 10$–$15\ \mu$m (Beule 2010), $r'_\mathrm{o} \sim 1$–5 mm (Proctor and Andersen 1982; Kirihene et al. 2002; Whyte and Boeddinghaus 2019), $\ell'_\mathrm{s} \sim 10$–30 mm (Whyte and Boeddinghaus 2019) and $\mathcal{V}'_\mathrm{s} \sim 10$–$20\ \mathrm{cm}^3$ (Cho et al. 2010; Yalcin et al. 2018). An estimate of V'_w can also be made by dividing the volumetric rate of mucus production in the nasal epithelium, by the area of the nasal epithelium. Gizurarson (2015) states that 20–40 mL of mucus is produced per day from around $160\,\mathrm{cm}^2$ of nasal mucosa; this yields an in-flow speed of $V'_\mathrm{w} \sim 0.015$–$0.03\ \mu$m/s. A third way to estimate V'_w is by noting that ciliary beating causes turnover of the mucus blanket every 20–30 min (Lund 1996); so, if the thickness of the mucus film is 10–15 μm, then V'_w should be $\sim 5 \times 10^{-3}\ \mu$m/s.

In our theoretical study, we will cover a broad range of values of $(U'_\mathrm{w}, V'_\mathrm{w})$ to reflect the wide variance in MCC rates across different sinus geometries and physiological conditions. We note that not all pairs of values of $(U'_\mathrm{w}, V'_\mathrm{w})$ would correspond to the typical conditions inside a healthy sinus. The lowermost values of U'_w would reflect MCC in sinuses characterised by extensive cilia loss, whereas the largest values of V'_w would be more representative of sinuses with mucosal swelling, a condition which leads to more mucus secretion (Whyte and Boeddinghaus 2019).

3 Active, Fluid-Producing Thin-Film Equations

The objective of our paper is to identify the physical conditions amenable to maintenance of a steady mucus layer inside the model sinus. We thus need to solve the equations governing mucus flow inside the sinus, and from them, deduce the shape of the mucus film. Since the typical thickness of the mucus layer $h' \sim 10$–$15\ \mu$m (Beule 2010) is much smaller than the typical length-scale of the sinus $\ell'_\mathrm{s} \sim 10$–30 mm (Whyte and Boeddinghaus 2019), the dynamics of mucus flow are governed by classical thin-film (lubrication) equations (Leal 2007). In this paradigm, the fluid's velocity normal to the sinus walls is at least $\epsilon = h'/\ell'_\mathrm{s}$ times smaller than its velocity along the sinus walls, where $\epsilon \ll 1$. Thus, the fluid flow is predominantly tangential to the sinus walls. In addition, the relative thinness of the mucus layer means that the variation of fluid velocity along the film is negligible as compared to its variation across the film. Finally, in the thin-film limit, the fluid pressure varies only along the film, while staying approximately constant normal to the film. These ideas are mathematically formalized in Appendices A.1 and B.1.

Under the simplifying assumptions listed above, a classical method may be used to derive the evolution equation satisfied by the mucus thickness (Leal 2007). One starts by expressing the (tangential) velocity of the fluid as a superposition of a pressure-driven flow resulting from variations in the height of the mucus film, a boundary-driven flow caused by the cilia-induced tangential velocity imposed along the cavity walls and

Table 1 Typical values of mucus properties and flow speeds $\left(U'_{\mathrm{w}}, V'_{\mathrm{w}}\right)$ (top) and important dimensionless numbers (bottom), corresponding to mucociliary clearance in humans (Silberberg 1983; Albers et al. 1996; Bull et al. 1999; Craster and Matar 2000; Smith et al. 2008; Lai et al. 2009; Hamed and Fiegel 2013; Chen et al. 2019; Patne 2024). Note that the value of u'_{c} used to non-dimensionalise $\left(U'_{\mathrm{w}}, V'_{\mathrm{w}}\right)$ (and other quantities) in the main text corresponds to $\mu = 10^{-1}$ kg m^{-1} s^{-1} and $\sigma = 0.08$ N m^{-1} (Smith et al. 2008)

Parameter	Description	Typical value	Units
ρ	Mucus density	10^3	kg m^{-3}
μ	Mucus viscosity	10^{-3} to 10	kg m^{-1} s^{-1}
σ	Mucus-air surface tension	0.01 to 0.1	N/m
h'	Mucus film thickness	10 to 15	μm
ℓ'_{s}	Sinus length-scale	10^{-2} to 3×10^{-2}	m
$\epsilon = \frac{h'}{\ell'_{\mathrm{s}}}$	Ratio of mucus film thickness to sinus length	10^{-3} to 10^{-2}	dimensionless
g	Gravitational force per unit mass	9.8	m s^{-2}
$u'_{\mathrm{c}} = \frac{\epsilon^2 \rho g \ell'^2_{\mathrm{s}}}{\mu}$	Reference velocity scale	10^{-3} to 10^4	μm s^{-1}
U'_{w}	Tangential velocity at the wall	1 to 400	μm s^{-1}
V'_{w}	Normal velocity at the wall	10^{-5} to 10^{-2}	μm s^{-1}
$\mathrm{Bo} = \frac{\rho g \ell'^2_{\mathrm{s}}}{\sigma}$	Bond number	≈ 12	dimensionless
$U_{\mathrm{w}} = \frac{U'_{\mathrm{w}}}{u'_{\mathrm{c}}}$	Normalised tangential velocity	10^{-1} to 40	dimensionless
$V_{\mathrm{w}} = \frac{V'_{\mathrm{w}}}{\epsilon u'_{\mathrm{c}}}$	Normalised wall-normal velocity	10^{-3} to 1	dimensionless

a flow driven due to gravity. This velocity can then be used to calculate the tangential flux (i.e. flow rate) of mucus, as a function of the local height of the mucus film. Thereafter, one can use a mass balance argument to relate the rate-of-change of the mucus film's height to the tangential mucus flux and the mucus production rate. In this way, the thin-film analysis allow us to reduce the multiple, coupled, nonlinear partial differential equations and boundary conditions describing the fluid's flow-field, into a single nonlinear, partial differential equation describing the time evolution of the height of the mucus film (Leal 2007). While the mathematical details of the derivation of these thin-film equations are shown in Appendices A.1 and B.1, we provide here the final, dimensionless equations governing the film thickness, in both circular and spherical geometries.

3.1 Circular Geometry

3.1.1 Governing Equation

In a symmetric system as shown in Fig. 2a, the (dimensionless) thickness of the mucus film obeys (see Appendix A.1 for details),

$$\frac{\partial H_{\mathrm{c}}}{\partial t} + \frac{\partial Q_{\mathrm{c}}}{\partial \theta_{\mathrm{c}}} = V_{\mathrm{w}}, \tag{4}$$

where,

$$Q_{\mathrm{c}}(\theta_{\mathrm{c}}, t) = \frac{H_{\mathrm{c}}^3}{3}\left[\frac{\epsilon}{\mathrm{Bo}}\frac{\partial}{\partial\theta_{\mathrm{c}}}\left(H_{\mathrm{c}} + \frac{\partial^2 H_{\mathrm{c}}}{\partial\theta_{\mathrm{c}}^2}\right) + \sin\theta_{\mathrm{c}}\right] + u_{\mathrm{w},\theta_{\mathrm{c}}}(\theta_{\mathrm{c}})\, H_{\mathrm{c}}(\theta_{\mathrm{c}}, t), \tag{5}$$

where the sub-script 'c' denotes circular geometry. In Eq. (4), $H_{\mathrm{c}}(\theta_{\mathrm{c}}, t)$ is the film thickness at location θ_{c} and time t, $Q_{\mathrm{c}}(\theta_{\mathrm{c}}, t)$ is the local, tangential fluid flux and V_{w} is the dimensionless normal component of the fluid velocity at the cavity wall. In Eq. (5), $\epsilon = h'/\ell'_{\mathrm{s}} \ll 1$ is the ratio of the characteristic film thickness h' to the characteristic length-scale of the sinus ℓ'_{s}; Bo is the Bond number, a dimensionless measure of the importance of gravity as compared to surface tension, in driving the film (see Appendix A.1). Also, $u_{\mathrm{w},\theta_{\mathrm{c}}}(\theta_{\mathrm{c}})$ in Eq. (5) is a prescribed tangential velocity at the walls of the circle (blue arrows in Fig. 2a), which models the action of the ciliated epithelium on the mucus; we discuss its functional form in Sects. 3.1.3 and 3.3.

3.1.2 Boundary Conditions

The symmetry of the setup in Fig. 2a means that we just need to solve Eq. (4) over half the domain, i.e. for $0 \le \theta_{\mathrm{c}} \le \pi$; where $\theta_{\mathrm{c}} = 0$ is the topmost point (orange dot in Fig. 2a) and $\theta_{\mathrm{c}} = \pi$ is the bottommost point (black dot in Fig. 2a); the solution for $\pi \le \theta_{\mathrm{c}} \le 2\pi$ can then be obtained by reflecting the solution for $0 \le \theta_{\mathrm{c}} \le \pi$ about the (vertical) axis. Symmetry also dictates that the flow-rate must vanish at $\theta_{\mathrm{c}} = \pi$, which yields the following conditions on $u_{\mathrm{w},\theta_{\mathrm{c}}}$ and H_{c}:

$$\begin{aligned} u_{\mathrm{w},\theta_{\mathrm{c}}}(\theta_{\mathrm{c}} = \pi) &= 0, \\ \left.\frac{\partial H_{\mathrm{c}}}{\partial\theta_{\mathrm{c}}}\right|_{\theta_{\mathrm{c}}=\pi} &= 0, \\ \left.\frac{\partial^3 H_{\mathrm{c}}}{\partial\theta_{\mathrm{c}}^3}\right|_{\theta_{\mathrm{c}}=\pi} &= 0. \end{aligned} \tag{6}$$

The first condition in Eq. (6) needs to be satisfied by design, by choosing a function $u_{\mathrm{w},\theta_{\mathrm{c}}}(\theta_{\mathrm{c}})$ that it is odd with respect to $\theta_{\mathrm{c}} = \pi$ (see Eq. (10), Sect. 3.3). The second and third conditions follow from symmetry and the condition of continuity of film shape at $\theta_{\mathrm{c}} = \pi$.

3.1.3 Modeling the Ostium

For the circular geometry, we model the ostium as a discontinuity in the fluid velocity at $\theta_{\mathrm{c}} = 0$, or equivalently, at $\theta_{\mathrm{c}} = 2\pi$. Our choice of a symmetric ciliary wall-slip that is odd with respect to $\theta_{\mathrm{c}} = \pi$ (shown qualitatively in Fig. 2a; see also Sect. 3.3), disrupts the periodicity of a circular geometry at $\theta_{\mathrm{c}} = 2\pi$; in fact, it causes a jump, such that $Q_{\mathrm{c}}(\theta_{\mathrm{c}} = 2\pi) = -Q_{\mathrm{c}}(\theta_{\mathrm{c}} = 0)$. However this is not a problem if we treat the point $\theta_{\mathrm{c}} = 0, 2\pi$ as a local sink of fluid flow. Thus, once the action of the wall-slip causes the fluid to reach $\theta_{\mathrm{c}} = 0, 2\pi$, the fluid is instantaneously removed from the domain/cavity, much like mucus exiting the sinus from its ostium.

3.2 Spherical Geometry

3.2.1 Governing Equation

For a spherical (but axisymmetric) geometry, the mucus film thickness satisfies (see Appendix B.1 for details),

$$\frac{\partial H_{\rm s}}{\partial t} + \frac{1}{\sin\theta_{\rm s}}\frac{\partial Q_{\rm s}}{\partial \theta_{\rm s}} = V_{\rm w}, \tag{7}$$

where,

$$\begin{aligned} Q_{\rm s}(\theta_{\rm s}, t) = \frac{H_{\rm s}^3 \sin\theta_{\rm s}}{3}\left[\frac{\epsilon}{\rm Bo}\frac{\partial}{\partial\theta_{\rm s}}\left(2H_{\rm s} + \frac{\partial H_{\rm s}}{\partial \theta_{\rm s}}\cot\theta_{\rm s} + \frac{\partial^2 H_{\rm s}}{\partial\theta_{\rm s}^2}\right) + \sin\theta_{\rm s}\right] \\ + u_{{\rm w},\theta_{\rm s}}(\theta_{\rm s})\, H_{\rm s}(\theta_{\rm s}, t)\sin\theta_{\rm s}, \end{aligned} \tag{8}$$

where the sub-script ‘s’ denotes spherical geometry. In Eq. (7), $Q_{\rm s}(\theta_{\rm s}, t)$ denotes the instantaneous, azimuthally averaged tangential flux at the location $\theta_{\rm s}$ (i.e. the tangential flux normal to the dotted line in Fig. 2b, averaged over the coordinate $\phi_{\rm s}$). Similar to Eq. (5), $u_{{\rm w},\theta_{\rm s}}(\theta_{\rm s})$ in Eq. (8) is a prescribed tangential velocity at the walls of the spherical cavity.

3.2.2 Boundary Conditions

In the 3D axisymmetric case, symmetry dictates that we must have at the bottom pole (at $\theta_{\rm s} = \pi$),

$$\begin{aligned} u_{{\rm w},\theta_{\rm s}}(\theta_{\rm s} = \pi) = 0, \\ \left.\frac{\partial H_{\rm s}}{\partial\theta_{\rm s}}\right|_{\theta_{\rm s}=\pi} = 0. \end{aligned} \tag{9}$$

Once again the first condition in Eq. (9) needs to be satisfied by a suitable choice of $u_{{\rm w},\theta_{\rm s}}$ (see Eq. (10), Sect. 3.3). We do not need any other boundary conditions because the flux $Q_{\rm s}$ vanishes identically, by definition, at the bottom pole (Kang et al. 2016; Qin et al. 2020).

3.2.3 Modeling the Ostium

In the 3D geometry, the fluid inside the cavity exits through an ostium modelled as a small, flat hole at the top, as marked by the orange circle in Fig. 2b. Note that it is essential to truncate the sphere, and we cannot have a discontinuity-based exit from the top pole of an un-truncated/complete sphere; since for $\theta_{\rm s} = 0$ the flow-rate $Q_{\rm s}$ vanishes identically and so it is (understandably) impossible to exit as the radius of the orange ring in Fig. 2b tends to zero. In the present work, the radius of the model ostium is defined by an exit angle $\theta_{\rm e} \sim \sin^{-1}\left(r_{\rm o}'/\ell_{\rm s}'\right)$ (see Fig. 2b), where $r_{\rm o}'$ and $\ell_{\rm s}'$

are, respectively, the typical ostium radius and the typical sinus length-scale. Using the values of r_o' and ℓ_s' as mentioned in Sect. 2.3, we obtain $\theta_e \approx 5^\circ - 20^\circ$.

3.3 Physical Description of the Thin-Film Equations

Physically, Eqs. (4) (2D) and (7) (3D) describe a mass-balance argument: the time-rate-of-change of film-height at any section (θ, t), is the sum of the net fluid flux entering the section tangentially ($-\partial Q_c/\partial\theta_c$ in Eq. (4) and $-(\sin\theta_s)^{-1}\,\partial Q_s/\partial\theta_s$ in Eq. (7)), and the fluid entering the section normally through the boundary, V_w. Then, Eqs. (5) (2D) and (8) (3D) describe the three contributions to the tangential fluid flux Q. The first is flow due to gravity, which is the term inside the square brackets that is proportional to $\sin\theta$ ($\theta = \theta_c$ or θ_s) in Eqs. (5) and (8). The second is the flow due to the effective action of the cilia, which is the last term in Eqs. (5) and (8). The third contribution is the flow due to a surface-tension-driven pressure gradient resulting from spatial changes in the film's curvature; this is the term multiplying ϵ/Bo in the square brackets.

The results in Eqs. (4) and (5) in 2D (and, Eqs. (7) and (8) in 3D) are extensions to the classical systems of equations governing thin-film dynamics over curved substrates (Oron et al. 1997; Craster and Matar 2009; Qin et al. 2020; McKinlay et al. 2023), with two important additions: a wall-normal fluid velocity contribution V_w in Eqs. (4) and (7), and an active tangential slip contribution $u_{w,\theta_{c/s}}\left(\theta_{c/s}\right)$ in Eqs. (5) and (8). In our model, these represent respectively, the production of mucus inside the sinus, and the sweeping of the mucus toward the ostium by the ciliated cells. In the limits of $u_{w,\theta_{c/s}} \equiv 0$ and $V_w \equiv 0$, our formulation reduces to the classical (passive) formulations for cylinders (McKinlay et al. 2023) and spheres (Qin et al. 2020).

As mentioned above, we assume that the mucus enters the system at a uniform rate V_w, normally at the wall. The spatial distribution of the tangential velocity, $u_{w,\theta}(\theta)$, is motivated by the observation that "*mucociliary transport begins in the maxillary sinus as a star, from the bottom of the sinus and moves in various directions towards the ostium*" (Drettner 1980) (see also Fig. 1c). This is modelled, for both Eqs. (5) and (8), by a hyperbolic tangent function,

$$u_{w,\theta}(\theta) = -U_w \tanh\left(\frac{\pi - \theta}{\pi \ell_c}\right), \quad \theta = \theta_c \text{ or } \theta_s, \tag{10}$$

such that the tangential slip is zero at the bottom-most point (see the black dots at the bottom in Fig. 2) and increases to U_w over a relevant length-scale ℓ_c, as we move up along the cavity. In the present work, we set $\ell_c = 0.5$, for a smooth transition from 0 at the floor of the cavity, to $\sim U_w$ near the ostium; lower values of ℓ_c, quantifying a more rapid spatial transition, have only a minor, quantitative effect on our main results. We note that for a circular geometry, this definition of $u_{w,\theta_c}(\theta_c)$ leads to a discontinuity at $\theta_c = 0, 2\pi$, such that $u_{w,\theta_c}(\theta_c = 0) = -u_{w,\theta_c}(\theta_c = 2\pi)$, but, as explained in Sect. 3.1.3, this is not a problem because $\theta_c = 0, 2\pi$ denotes a fluid sink for the 2D geometry, and hence allows for discontinuity of the wall velocity.

3.4 Numerical Solution and Validation

We numerically solve Eqs. (4) and (7), with the boundary conditions (6) and (9) respectively, using a semi-implicit finite-difference method whose details are provided in Appendices A.2 and B.2. We validate our numerical solution in the limit of zero mucus production ($V_{\mathrm{w}} \equiv 0$) and sweeping ($U_{\mathrm{w}} \equiv 0$), by reproducing classical results of the drainage of a thin film over a cylindrical (McKinlay et al. 2023) and a spherical (Qin et al. 2020) substrate, as shown in Figs. 11a and 12a in Appendices A and B, respectively.

4 Steady Mucus Drainage in Active Fluid-Producing Thin Films

We begin our results with a comment on the dimensionless values of $(U_{\mathrm{w}}, V_{\mathrm{w}})$, whose corresponding dimensional values $\left(U'_{\mathrm{w}}, V'_{\mathrm{w}}\right)$ were discussed in Sect. 2.3. A natural velocity scale in the present problem is set by gravity, $u'_{\mathrm{c}} = \epsilon^2 \rho g \ell'^2_{\mathrm{s}}/\mu$ (see Appendix A.1), where μ is the fluid's dynamic viscosity, whose range of values is given in Table 1. This is the characteristic velocity with which a thin film would flow down a substrate due to gravity alone. In the thin-film analysis, the fluid velocities tangential and normal to the surface are made dimensionless using u'_{c} and $\epsilon u'_{\mathrm{c}}$, respectively, which yields (with $\epsilon = 10^{-3}$ and $u'_{\mathrm{c}} \approx 10\ \mu$m/s; see Table 1):

$$
\begin{aligned}
U_{\mathrm{w}} &= \frac{\mu U'_{\mathrm{w}}}{\epsilon^2 \rho g \ell'^2_{\mathrm{s}}} \approx 0.1 \text{ to } 40, \\
V_{\mathrm{w}} &= \frac{\mu V'_{\mathrm{w}}}{\epsilon^3 \rho g \ell'^2_{\mathrm{s}}} \approx 0.005 \text{ to } 2.
\end{aligned} \tag{11}
$$

4.1 Mucus Film Evolution in Two Dimensions

We illustrate in Fig. 3 two representative examples of the time evolution of the (thin) mucus film in a circular cavity, i.e. in two dimensions. In Fig. 3a (Cartesian plot) and b (polar plot), the active wall-slip (ciliary action) is not sufficiently strong to push out the fluid that is being produced in the cavity walls. Hence, the fluid inside the sinus increases in volume with time and, due to gravity, it accumulates at the bottom. This results in a progressive increase in the film height at the bottom of the cavity, until the thin-film approximation breaks down and the situation becomes non-representative of mucus flow inside sinuses. However, if the magnitude of the tangential slip, U_{w}, is increased beyond a threshold, then one does obtain a steady solution, as shown in Fig. 3c and d. In this case, the active motion (U_{w}) is sufficiently large to overcome gravity; it then drives the fluid out of the cavity and balances the local fluid production (V_{w}), leading to the development of a thin mucus layer, as is expected inside healthy sinuses.

For the cases where a steady thin film can be obtained (i.e. when U_{w} is sufficiently large), the shape of the film as a function of the wall-slip, is shown in Fig. 4a. As expected from intuition, larger values of the characteristic slip U_{w}, result in thinner

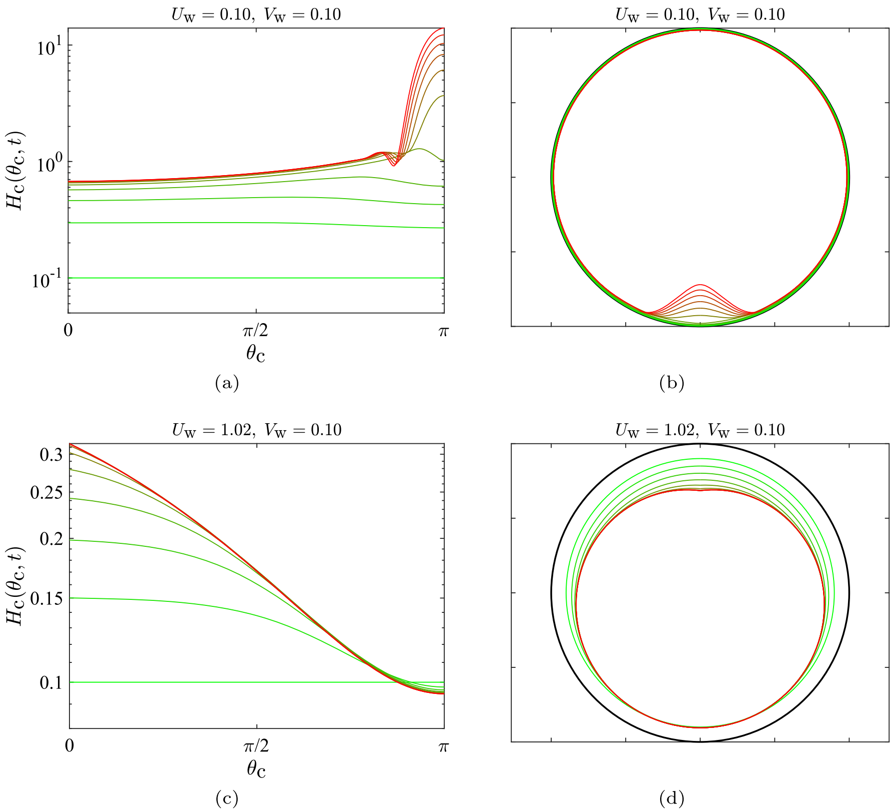

Fig. 3 The two regimes for the time evolution of the thin (mucus) film inside a circular cavity. **a**, **b** Time evolution of the film for $U_w = 0.10$ and $V_w = 0.10$, for which Eq. (4) does not have a steady solution; panel (**a**) is a Cartesian plot, and panel (**b**) is a polar plot where the film thickness has been magnified 20 times the actual value, to help visualisation. The profiles evolve from dimensionless time $t = 0$ (green) to $t = 20$ (red) in time intervals $\Delta t = 2$. **c**, **d** Time evolution of the film inside the circular cavity for $U_w = 1.02$ and $V_w = 0.10$, for which Eq. (4) reaches a steady solution; panel (**c**) is a Cartesian plot and panel (**d**) is a polar plot where the film thickness has been magnified 1000 times the actual value. The profiles evolve from dimensionless time $t = 0$ (green) to $t = 5$ (red) in time intervals $\Delta t = 0.5$. For these set of results, we considered $\ell_c = 0.3$

films (for a fixed rate of fluid injection V_w). We can obtain an expression for the exit-height of the film, $H_c(0)$, in terms of (U_w, V_w) by integrating Eq. (4), ignoring the contribution from the ϵ/Bo term ($\epsilon/\mathrm{Bo} \approx 8 \times 10^{-5} \ll 1$ throughout the paper; see Table 1), and noting that in steady state,

$$\frac{\partial}{\partial t}\int_0^{\pi} H_c(\theta_c, t)\, d\theta \equiv \frac{dV_{\mathrm{film}}}{dt} = 0,$$

where, V_{film} is the volume of the mucus film. This yields,

$$H_c(0) = \frac{\pi V_w}{U_w \tanh(\ell_c^{-1})}, \tag{12}$$

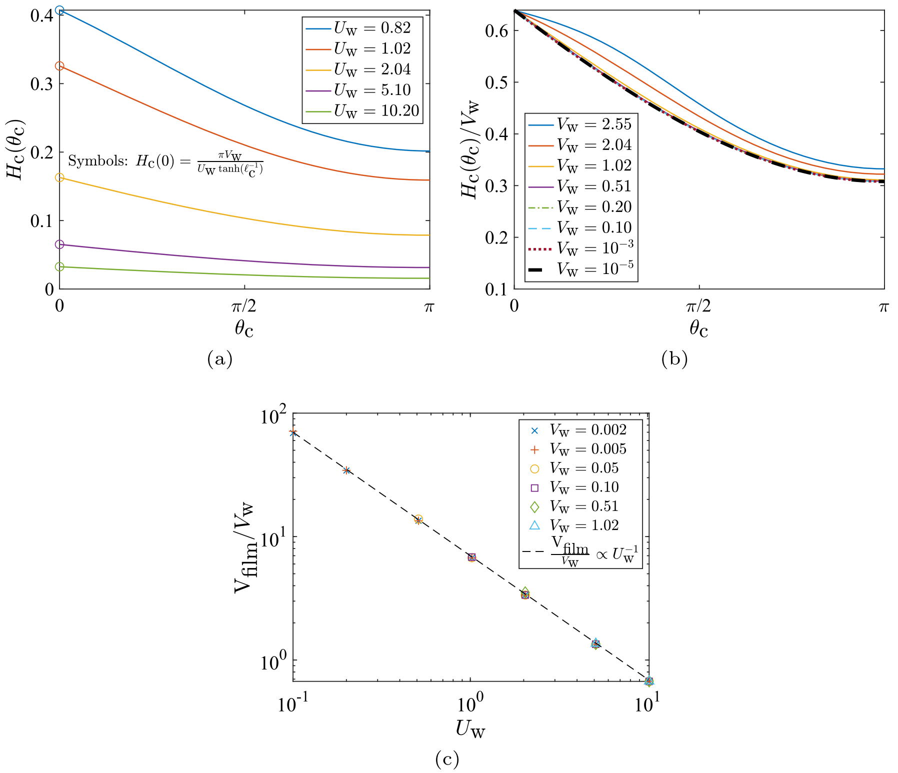

Fig. 4 Height of steady-state film in the two-dimensional geometry as function of active parameters U_W and V_W. **a** Variation of the film height for a two-dimensional/circular cavity, as a function of the effective ciliary clearance speed, U_W, for a fixed mucus injection rate $V_\mathrm{W} = 0.10$. **b** Steady-state film height normalised by the rate of mucus injection, $H_\mathrm{c}(\theta_\mathrm{c})/V_\mathrm{W}$, for different values of the injection rate; $U_\mathrm{W} = 5.10$ for all the plots. **c** Scaling of the film volume, V_film, with the injection rate, V_W, and the speed of ciliary clearance U_W, for low values of the injection rate

a prediction that is indeed confirmed by our numerics, as shown by the circles in Fig. 4a. Interestingly, Eq. (12) tells us that the steady-state exit-height in our problem does not depend on the fluid's properties (via the Bond number $\mathrm{Bo} = \rho g \ell_\mathrm{s}'^2/\sigma$) and depends only on the specified kinematics through $(U_\mathrm{W}, V_\mathrm{W}, \ell_\mathrm{c})$. Since it was necessary to neglect the ϵ/Bo term in order to arrive at Eq. (12), this means that surface tension plays a negligible role in film dynamics for the cases where a steady solution exists to Eq. (4).

In Fig. 4b we next show the normalised steady-state film shape, $H_\mathrm{c}(\theta_\mathrm{c})/V_\mathrm{W}$; of course, such a representation is valid only for $V_\mathrm{W} \neq 0$. It is clear that the average film-thickness increases monotonically with increasing V_W. For the lower-most values of V_W considered, the steady-state plots of $H_\mathrm{c}(\theta_\mathrm{c})/V_\mathrm{W}$ collapse onto each other; this is true for V_W as low as 10^{-5}. One may then write, $H_\mathrm{c}(\theta_\mathrm{c}) \approx V_\mathrm{W} \times f(\theta_\mathrm{c}; U_\mathrm{W}, \ell_\mathrm{c})$, for a large range of mucus production rates: $10^{-5} \leq V_\mathrm{W} \lesssim O(1)$.

If we postulate that the film volume V_film is proportional to the exit height $H_\mathrm{c}(0)$, then based on Eq. (12) we may conclude that the normalised film volume, $V_\mathrm{film}/V_\mathrm{W}$, is inversely proportional to the ciliary slip U_w; this is indeed confirmed numerically in Fig. 4c. We thus obtain a scaling estimate of the amount of mucus maintained inside the two-dimensional cavity, for rates of mucus injection that admit a steady solution over a large range of effective ciliary clearance strengths.

4.2 Mucus Film Evolution Inside a Sphere (Three Dimensions)

We now consider the three-dimensional case and show in Fig. 5 the time evolution of the mucus film inside the spherical cavity. The parameters in Fig. 5a and b correspond to the case where U_w is not sufficiently large to overcome gravity and Fig. 5c and d corresponding to the case where the active flow U_w is strong enough that a steady state can be reached. Both the unsteady and steady-state film shapes in the spherical case are qualitatively different from the circular case and there is a sharper increase in the film height (toward the bottom for the unsteady solutions in Fig. 5a and b, and also toward the top for the steady solution in Fig. 5c and d). In particular, the steady-state mucus film collects fluid as it develops from the bottom to the top of the cavity; and since the fluid must exit from a narrow constriction at the top, the film thickens much more rapidly than in the circular case.

The steady-state exit height, denoted by $H_s(\theta_e)$, is related nonlinearly to (U_w, V_w) via,

$$\left[-\frac{H_s^2}{3}\sin\theta_e + U_w \tanh\left(\frac{\pi-\theta_e}{\pi\,\ell_c}\right)\right] H_s \sin\theta_e = V_w\,(1+\cos\theta_e)\,, \tag{13}$$

which can be derived by ignoring the surface tension contribution in Eq. (7) (because $\epsilon/\mathrm{Bo} \ll 1$), multiplying its steady version by $\sin\theta_s$ and integrating from $\theta_s = \theta_e$ to $\theta_s = \pi$. For $H_s(\theta_e) \lesssim O(1)$ and $\theta_e \ll 1$, Eq. (13) yields,

$$H_s\,(\theta_e) \approx \frac{V_w}{U_w \tanh\left(\frac{\pi-\theta_e}{\pi\,\ell_c}\right)} \frac{(1+\cos\theta_e)}{\sin\theta_e}, \tag{14}$$

which is compared against the numerical results in Fig. 6, where we see that the analytical prediction best matches the numerical results for the thinner films and a mismatch occurs mainly when the exit height is not small, $H_s(\theta_e) \sim O(1)$. For $(U_w = 5.10, V_w = 1.02)$ in Fig. 6b, Eq. (14) overestimates the exit height because it ignores the contribution from surface-tension-induced pressure gradients. The latter become important near the exit, where rapid mucus accumulation results in sufficiently large gradients in the mucus film thickness, causing surface-tension-driven flows that reduce the exit height. Note that this role of surface tension is unique to the spherical geometry and is not seen for the circular geometry. The analytical estimate of the exit height for the circular geometry (Eq. (12)) also ignored surface tension, but it matched perfectly with the numerical results for a wide range of (U_w, V_w) (Fig. 4a). Thus, for the biologically-relevant values listed in Table 1, surface tension effects are truly negligible for the 2D/circular geometry, but this is not always the case for the 3D/spherical geometry.

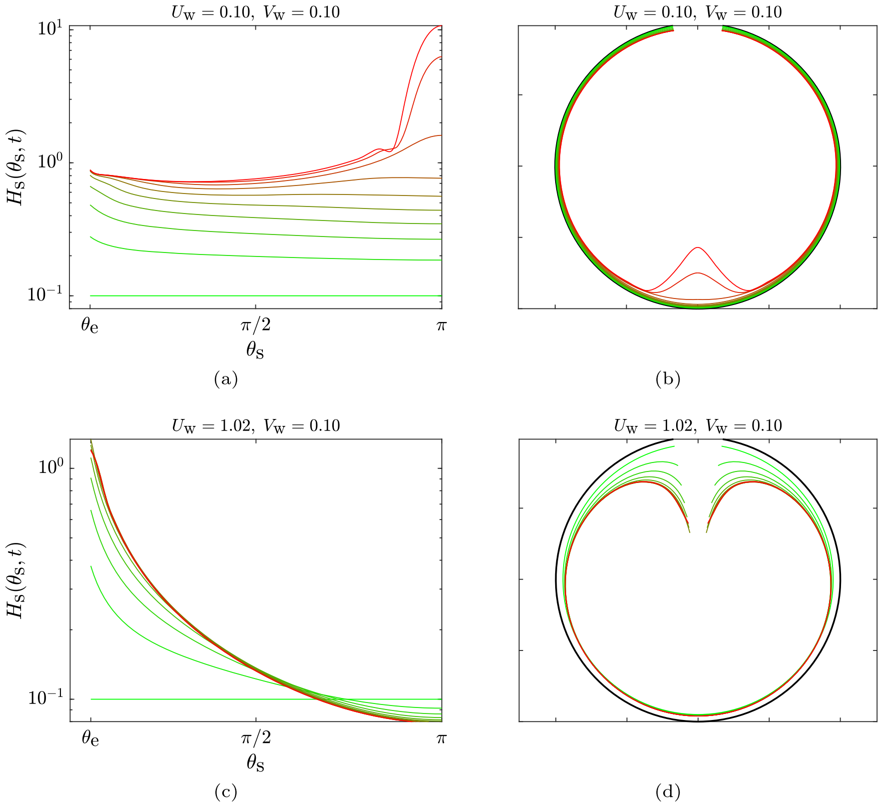

Fig. 5 Time evolution of the film inside the spherical cavity. **a**, **b** Case with $U_\mathrm{W} = 0.10$ and $V_\mathrm{W} = 0.10$, for which Eq. (7) does not have a steady solution; panel (**a**) is a Cartesian plot, and panel (**b**) is a polar plot where the film thickness has been magnified 40 times the actual value, for visualisation purposes. The profiles evolve from dimensionless time $t = 0$ (green) to $t = 9$ (red) in time intervals $\Delta t = 1$. **c**, **d** Case with $U_\mathrm{W} = 1.02$ and $V_\mathrm{W} = 0.10$, for which eqn. (7) reaches a steady solution; panel (**c**) is a Cartesian plot, and panel (**d**) is a polar plot where the film thickness has been magnified 500 times the actual value. The profiles evolve from $t = 0$ (green) to $t = 4.80$ (red) in time intervals $\Delta t = 0.4$. For these set of results, we considered $\ell_\mathrm{c} = 0.5$

5 Existence of a Steady Solution

5.1 Phase Space of Solutions

In the previous sub-section, we demonstrated that depending on the relative values of $(U_\mathrm{W}, V_\mathrm{W})$, the mucus film either builds up at the bottom of the cavity, or attains a steady-state shape wherein the mucus is cleared from the cavity at the same rate that it is produced at the cavity walls. This was the case both in two and three dimensions.

Using our numerical model, we can systematically vary the two active parameters, U_W and V_W, and map out the existence of these two different solutions. The results are shown in Fig. 7a for a circular (2D) cavity and in Fig. 7b for a spherical (3D) geometry with exit angle $\theta_\mathrm{e} = 5°$.

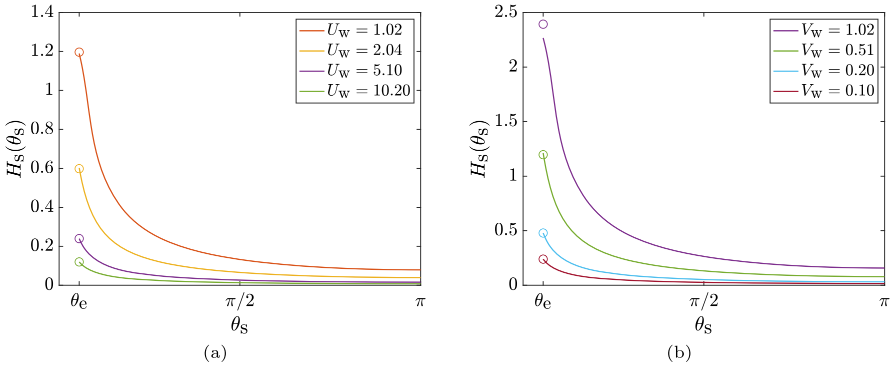

Fig. 6 Height of steady-state film in the three-dimensional geometry as function of active parameters U_W and V_W. **a** Film height as a function of the effective ciliary clearance speed, U_W, for a fixed mucus injection rate $V_W = 0.10$. **b** Film height as a function of the mucus injection rate, V_W, for a fixed effective ciliary clearance speed $U_W = 5.10$. The circles denote the analytical estimate of the exit height, based on Eq. (14)

As expected, a steady solution exists whenever the rate of mucus in-flow (V_W) is particularly low, or the effective ciliary velocity (U_W) is sufficiently high. The principal effect of the cavity geometry (circular versus spherical) is reflected in the slightly larger region of existence of steady solutions for the circular case. However, the general shape of the boundary demarcating steady and unsteady solutions remains unchanged between the circular and the spherical case. This suggests that the existence of a steady solution is due to the same fundamental physics in both geometries, which we rationalise below.

5.2 Steady vs Unsteady Solutions: Scaling Analysis

We now estimate the relation between U_W and V_W which defines the boundary between the steady and unsteady solutions in Fig. 7a and b, i.e. we derive a scaling between U_W and V_W for which Eqs. (4) and (7) are expected to admit a steady solution.

We start by a sketch of a typical section of the film, shown in Fig. 7c, highlighting the three relevant velocity scales governing the shape of the mucus film: fluid is produced at the walls at a rate V'_W, from where its motion is governed by a competition between a typical gravitational drainage velocity u'_c and an effective ciliary velocity U'_W, which tries to drive the fluid up and out of the cavity. Conservation of mass in the classical thin-film limit sets the relative scaling of U'_W and V'_W as,

$$\frac{U'_W}{\ell'_S} \sim \frac{V'_W}{h'},$$
$$\text{or,}\quad V'_W \sim \epsilon U'_W, \tag{15}$$

where we have used $h'/\ell'_S \sim \epsilon \ll 1$. Further, we argue that the active (ciliary) wall-velocity U'_W must be greater than the characteristic gravitational velocity scale $u'_c = \epsilon^2 \rho g \ell'^2_S/\mu$, in order to successfully drive the mucus out of the cavity, meaning, we require

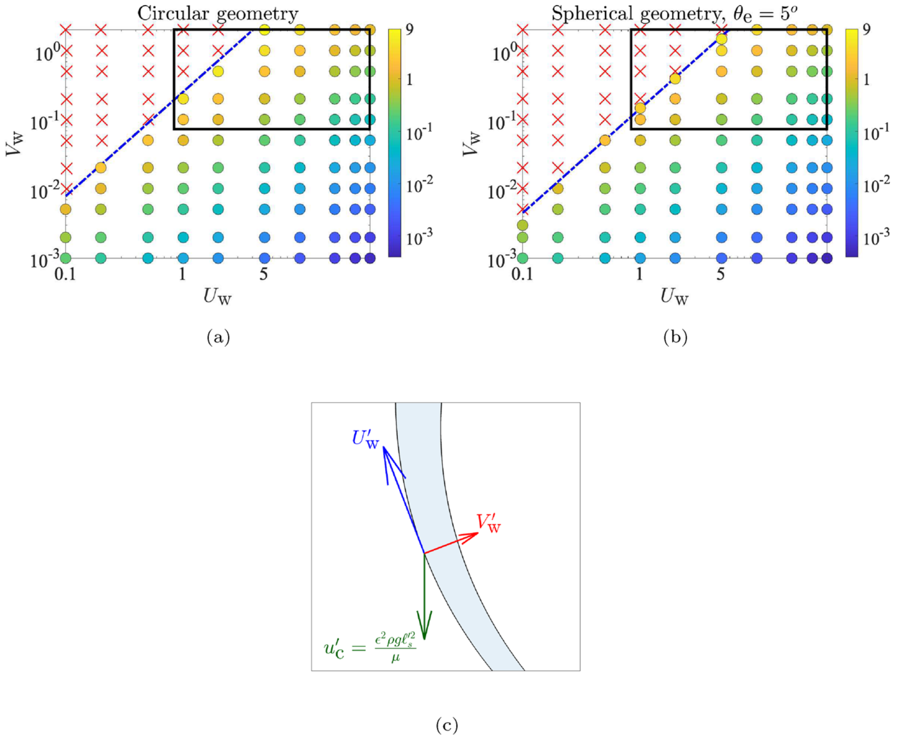

Fig. 7 Phase space of steady (∘) vs unsteady (×) solutions as a function of (U_W, V_W) for, **a** the circular geometry and **b** spherical geometry with $\theta_e = 5°$. The red crosses (×) denote cases where mucus accumulates inside the cavity, whereas the coloured circles (∘) denote cases where a steady mucus layer is formed, with colours quantifying the steady-state film volume normalised by the initial film volume. The blue line represents the transition scaling $V_W \propto U_W^{3/2}$ as predicted by Eq. (18). The black rectangle denotes the estimated range of values of U_W and V_W for human sinuses in healthy conditions. **c** Sketch of a magnified view of the mucus film and the three relevant velocities that govern the evolution of its shape

$$U'_W > \frac{\epsilon^2 \rho g \ell_s'^2}{\mu}. \tag{16}$$

The scalings in Eqs. (15) and (16) can be combined to yield,

$$U_W'^3 > \frac{\rho g \ell_s'^2}{\mu} V_W'^2, \tag{17}$$

which can be non-dimensionalised using the appropriate velocity scales in the thin-film limit (see beginning of Sect. 4 and Eq. (11)) to obtain,

$$U_W^3 > V_W^2 \quad \text{or} \quad V_W < U_W^{3/2}. \tag{18}$$

The resulting scaling $V_W \propto U_W^{3/2}$ from Eq. (18) has been plotted in Fig. 7, where we see that it aligns well with the boundary demarcating the unsteady solutions from the steady solutions, for both the circular (Fig. 7a) and the spherical system (Fig. 7b). Thus, the threshold clearance velocity required to obtain a steady mucus layer, say U_w^*, scales as the 2/3rd power of the rate of mucus in-flow, i.e. $U_w^* = kV_w^{2/3}$ (by inverting Eq. (18)), where the constant k can be determined from numerical solutions to Eqs. (4) and (7).

6 Application to Mucociliary Clearance in Human Sinuses

Using our theoretical model, we have identified the hydrodynamic conditions, specified by values of (U_w, V_w), under which a steady mucus layer can exist inside the cavity. Based on the discussions in Sect. 2.3, the operative conditions inside a healthy sinus correspond to an effective ciliary velocity, U_w' in the range 30 to 400 μm/s and the mucus in-flow V_w' in the range 5×10^{-3} to 3×10^{-2} μm/s. Using the characteristic velocity scales defined in the beginning of Sect. 4, the dimensionless values of the operative ciliary velocity and the mucus in-flow rate are thus given by $U_w \sim 1-40$ and $V_w \sim 0.5-3$. The region of the solution space that lies within this range is shown as rectangles in Fig. 7a and b. We see that, in general, these values do correspond to the existence of a steady solution according to our model. We thus postulate that the primary factors responsible for maintaining a steady mucus layer inside a healthy sinus are a combination of (i) the rate of mucus flow due to ciliary beating being sufficiently fast to overcome local gravitational drainage, and (ii) the rate of mucus production per unit area of the sinus being sufficiently small (as compared to the rate of ciliary clearance). Diseased conditions, such as excessive cilia loss or mucosal inflammation, violate one or both requirements, and thus, according to our model, will not lead to the formation of a thin mucus film over the sinus (Whyte and Boeddinghaus 2019).

It is estimated that it takes 20–30 min to replenish the mucus film during MCC, although this time varies significantly, even in healthy individuals (Lund 1996). We may use our model to compute the time t_r' taken to reach the steady-state from an initially small film height, $H_s(t=0) = 10^{-3}$, for values of (U_w, V_w) that fall within the physiological range outlined in Fig. 7b. This is illustrated for three cases in Fig. 8 and that time is seen to vary from $t_r' \approx 6$ min (when $(U_w \approx 40, V_w \approx 2)$) to $t_r' \approx 160$ min (when $(U_w \approx 1, V_w \approx 0.1)$). For $(U_w \approx 10, V_w \approx 1)$, values that lie in the middle of the physiological range, we obtain $t_r' \approx 20$ min. Thus, in addition to predicting the healthy operating conditions, our model is also able to approximately recover the typical mucus turnover rates observed in humans, under normal conditions.

An important geometric factor that affects mucus transport out of the sinuses is the size of the sinus opening, or the ostium. By varying θ_e in our 3D model, we can obtain further insight on the influence of the ostium size on mucus clearance. Typical ostium diameters range from 2–10 mm (Proctor and Andersen 1982; Kirihene et al. 2002; Whyte and Boeddinghaus 2019), which means that for a characteristic sinus length-scale $\ell_s' \sim O(1)$ cm (Whyte and Boeddinghaus 2019), the exit angle θ_e ranges from 5°-20°. The solution space for $\theta_e = 5°$ is compared with that for $\theta_e = 20°$ in Fig. 9. We see that there do exist instances in the (U_w, V_w) space where the fluid/mucus does not get cleared from the cavity with the narrower opening but it does get cleared

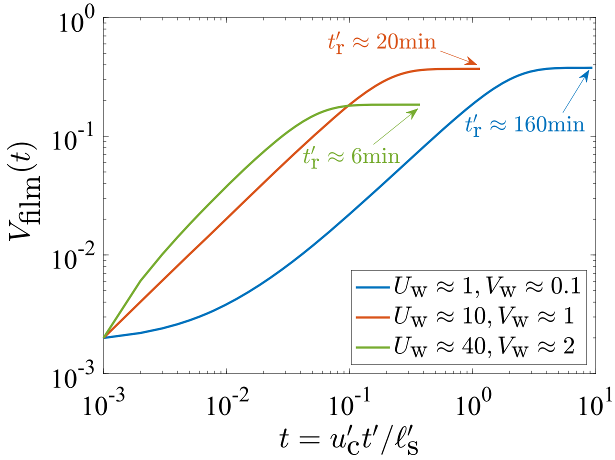

Fig. 8 Time-evolution of film volume until steady state is reached, for three values of the pair (U_w, V_w). The steady-state is considered to have been reached when the absolute rate of change of film volume falls below a threshold, $\left|\dot{V}_{film}(t)\right| \leq 10^{-5}$. The dimensional time at which the steady-state is reached, denoted by t'_r, is indicated for each case. Note that the horizontal axis shows the dimensionless time; the characteristic time-scale is given by $\ell'_s/u'_c \approx 17$ min

from the cavity with a larger opening; these are identified in Fig. 9 by the filled red squares (representing results for $\theta_e = 5°$) which coincide with the empty green circles (representing results for $\theta_e = 20°$). Overall, however, an increase in the ostium radius is seen to cause only a modest change in the nature of the solution space.

Interestingly, diseased sinuses appear to be accompanied by other pathologies such as nasal polyps, which are benign, painless growths in and around the sinuses that obstruct mucociliary clearance by blocking the ostium. This condition can be treated by surgically removing the polyps, unblocking the ostium and restoring smooth mucus flow out of the sinuses. Our model also hints at the efficacy of polyp-removal surgeries: it shows that an increase in the size of the ostium from $\theta_e = 5°$ to $\theta_e = 20°$ (see Fig. 2b) doubles the maximum value of the mucus production rate, say $V_{w,max}$, for which a steady mucus layer can exist inside the cavity. For example, Fig. 9 shows that, for $U_w \approx 2$, $V_{w,max} \approx 0.2$ when $\theta_e = 5°$ but it increases to $V_{w,max} \approx 0.5$ when θ_e is increased to 20°. Similar 2-fold increments in $V_{w,max}$ can be seen for other values of U_w as well, whenever θ_e is increased from 5° to 20°.

7 Conclusion and Perspectives

7.1 Summary of Modelling

We considered in this paper the problem of thin-film fluid flow inside circular (2D) and spherical (3D) cavities, as a model for active mucociliary clearance (MCC) in the maxillary sinuses. Building on classical work for passive thin films, we derived a new nonlinear, partial differential equation for the time evolution of a thin film of

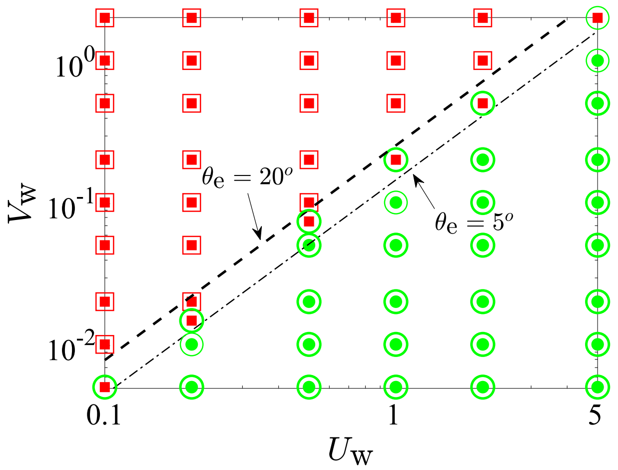

Fig. 9 Effect of varying ostium size, quantified by the exit angle θ_e (see Fig. 2b), on the solution space in 3D model. Empty symbols are used to denote the solution type for the case with the broader exit angle ($\theta_e = 20°$) whereas filled symbols denote the solution type for the case with the narrower exit angle ($\theta_e = 5°$). There exists a small range (between the thin dash-dotted line and the thick dashed line) where solutions for $\theta_e = 5°$ (filled red squares) are unsteady but the solutions for $\theta_e = 20°$ (empty green circles) are steady

fluid (mucus) that is released from the walls of a cavity (sinus) and driven, against gravity, toward an exit (ostium) by ciliary pumping, which is modelled as a prescribed tangential velocity at the cavity walls (active slip). Numerical solutions to this equation reveal two different behaviours in the long term: the mucus can either build up progressively at the bottom of the cavity or be cleared out at the same average rate with which it is produced, leading to the formation of a thin, steady film lining the cavity. These two regimes are demarcated on a phase-space of solutions (see Fig. 7a in 2D and b in 3D) defined by the rate of mucus production (denoted, in dimensionless form, as V_w) and the rate of mucus clearance by cilia (U_w, in dimensionless form). The fate of the mucus is decided by the relative magnitudes of U_w and V_w. Using a scaling analysis based on physical arguments, we showed show that the threshold clearance velocity required to obtain a steady mucus layer scales as 2/3$^{\text{rd}}$ power of the rate of mucus in-flow, i.e. the line separating the steady and unsteady solutions in Fig. 7a and b is given by $U_w = kV_w^{2/3}$, with a constant k that depends on the system geometry.

7.2 Summary of Biological Relevance

Biologically, mucus is produced in the sinuses at a rate $V'_w \sim 0.005$ to 0.03 μm/s, due to hydration of mucins secreted by goblet cells. The cilia push this mucus out of the sinuses with a velocity in the range $U'_w \sim 30$ to 400 μm/s. For typical values of the physical properties of mucus (see Table 1), the intrinsic gravitational drainage/settling velocity is $u'_c \sim 10$ μm/s. These values correspond to a healthy sinus, and hence they must lead to emergence of a steady state in our model system. This is indeed the case, most notably for the larger values of U'_w, as shown in Fig. 7. Our theoretical model thus captures the essential physical ingredients responsible for successful mucociliary clearance, particularly in the maxillary sinus, where it is known that the cilia must work against gravity to deliver mucus to the nasal cavity (Bluestone et al. 2012; Butaric et al. 2018; Whyte and Boeddinghaus 2019; Kim et al. 2021).

7.3 Model Extensions

Our model uses many assumptions, which could be relaxed in future studies. Firstly, the ostium of the maxillary sinus isn't always located at the highest point in the cavity and is often located on a medial wall (Whyte and Boeddinghaus 2019). In terms of the present model, this would amount to a rotation of the gravity vectors shown in Fig. 2, leading to loss of axisymmetry in the spherical case. When the ostium is not located symmetrically as shown in Fig. 2b, one can develop and solve a non-axisymmetric thin-film equation for the time evolution of the film height as a function of the polar (θ_{s}) and azimuthal (ϕ_{s}) angles. This would require a conceptually straightforward, albeit numerically cumbersome, extension of the current work; where a key step would be to identify the form of the ciliary slip, $u_{\mathrm{w},\theta_{\mathrm{s}}}(\theta_{\mathrm{s}}, \phi_{\mathrm{s}})$ (see Eq. 8).

Secondly, we treat the mucus as a single Newtonian fluid, whereas in reality it is a bi-layered, viscoelastic and shear-thinning fluid (Knowles and Boucher 2002; Button et al. 2012). The non-Newtonian rheology of the mucus will cause it to react differently to the ciliary slip than a Newtonian (purely viscous) fluid. These effects may significantly change the structure of the thin film equations (Eqs. (4)–(8)), hence the shape of the mucus film inside the cavity and likely the phase-space of solutions in Fig. 7.

Thirdly, the maxillary sinus has a very complex geometry that isn't fully captured by any one regular shape. It is often described to be pyramidal, and characterised by geometrical features such as recesses and protrusions (Whyte and Boeddinghaus 2019). Hence, an investigation of the influence of the actual sinus shape on MCC must extend the current work to cavities containing one or more of these features. Initial progress along this direction can be made for shapes that are small deviations from a sphere/circle, but analysis for more realistic shapes would necessitate the use of extensive computations.

The agreement between our predictions of steady-state operating conditions in sinuses and existing estimates of mucociliary clearance rates (Fig. 7b), shows that our model successfully captures the key physical mechanism responsible for uninterrupted mucus flow in the sinuses, and is thus encouraging. However, the simplicity of our model can restrict certain quantitative comparisons with real systems, for example, on aspects related to spatial variation of the film shape and the total volume of mucus contained in the film. Thus, further investigations of mucociliary clearance in sinuses are warranted to fully explore the appropriate physical conditions required to maintain healthy sinuses.

Appendix A: 2D/Circular System

See Fig. 10

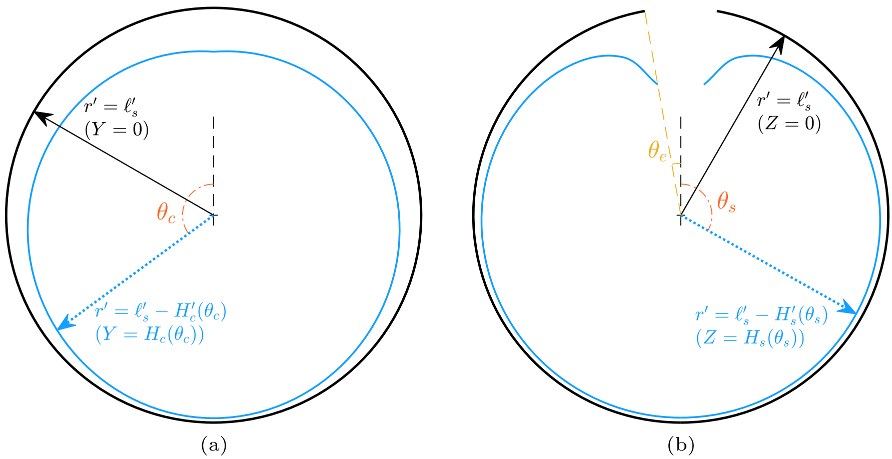

Fig. 10 Sketch of the dimensional coordinate system used to describe **a** the circular cavity/sinus, and, **b** the spherical cavity/sinus. The black, solid arrow identifies the walls (black circle) and the blue, dotted arrow identifies the free surface (blue curve) of the fluid/mucus. Note that panel (**a**) is a planar/2D geometry ($0 \le \theta_c \le 2\pi$), whereas panel (**b**) is a section of an otherwise 3D geometry ($\theta_e \le \theta_s \le \pi$); see also Fig. 2

A.1 Derivation of the Thin-Film Equation

The fluid flow inside the sinus is dominated by viscous forces (i.e. the inertia of the fluid is negligible), and hence is governed by the Stokes equations and the incompressibility condition (i.e. continuity equation) (Leal 2007). For the 2D/circular system, we will work in polar coordinates $\left(r', \theta_c, z'\right)$. Since we are interested in a planar flow, the z'-component of the velocity and all derivatives with respect to the z'-coordinate are identically zero, i.e. $u'_z \equiv 0$ and also $\partial(\ )/\partial z' \equiv 0$.

The system geometry is described in Fig. 10a, where the walls of the cavity/sinus are at $r' = \ell'_s$ and the free surface of the fluid/mucus film is at $r' = \ell'_s - H'_c(\theta_c, t)$. The starting point for deriving Eq. (4) is to non-dimensionalise the equations governing fluid flow in polar coordinates using the following reference scales:

$$
\begin{aligned}
r' &= \ell'_s (1 - \epsilon Y), \\
H'_c &= \epsilon \ell'_s H_c, \\
u'_{\theta_c} &= u'_c u_{\theta_c}, \\
u'_r &= \epsilon u'_c u_r, \\
t' &= \frac{\ell'_s}{u'_c} t,
\end{aligned}
$$

$$p' = \epsilon^{-2} \frac{\mu u_c}{\ell'_s} p. \tag{A1}$$

In the above, $\epsilon = h'/l'_s \ll 1$ is a small parameter defined as the ratio of the typical thickness of the mucus film to the typical length-scale of the sinus. The coordinate Y is a local stretched coordinate normal to the boundary; $Y = 0$ denotes the cavity wall and $Y = H_c$ denotes the free surface of the fluid. Note that the reference scales defined above correspond to the classical thin-film approximation over curved substrates (Oron et al. 1997; Craster and Matar 2000; Leal 2007). Note also that we have purposely defined a generic velocity scale u'_c, to show how the velocity scale emerges naturally from the equations governing fluid flow.

After the governing equations are rendered dimensionless using (A1), we identify the dominant balance in each equation by retaining only the leading order terms, i.e. the terms in each equation with the lowest powers of ϵ. This yields the continuity equation in the thin-film limit,

$$-\frac{\partial u_r}{\partial Y} + \frac{\partial u_{\theta_c}}{\partial \theta_c} = 0, \tag{A2}$$

the dimensionless r'-momentum (or, Y-momentum) equation in the thin-film limit,

$$\frac{\partial p}{\partial Y} - \epsilon^3 \frac{\rho g \ell_s'^2}{\mu u'_c} \cos\theta_c = 0, \tag{A3}$$

and the dimensionless θ_c-momentum equation in the thin-film limit,

$$-\frac{\partial p}{\partial \theta_c} + \frac{\partial^2 u_{\theta_c}}{\partial Y^2} + \epsilon^2 \frac{\rho g \ell_s'^2}{\mu u'_c} \sin\theta_c = 0. \tag{A4}$$

Eq. (A4) provides the characteristic velocity scale,

$$u'_c = \epsilon^2 \frac{\rho g \ell_s'^2}{\mu}, \tag{A5}$$

that we employ in all our derivations. Using this scale, Eqs. (A3) and (A4) simplify to:

$$\frac{\partial p}{\partial Y} \sim O(\epsilon) \approx 0, \tag{A6}$$

and,

$$-\frac{\partial p}{\partial \theta_c} + \frac{\partial^2 u_{\theta_c}}{\partial Y^2} + \sin\theta_c = 0. \tag{A7}$$

The system in Eqs. (A2), (A6) and (A7) is supplemented by: (i) boundary conditions (BCs) for the fluid velocity $\left(u_{\theta_c}, u_r\right)$ at the walls of the circle, (ii) BCs for the fluid stress at the free surface of the thin film, and, (iii) a kinematic boundary condition relating the fluid's velocity at the free surface to the film deformation. The first of these set of BCs is given by:

$$u_{\theta_c}\big|_{Y=0} = -U_w \tanh\left(\frac{\pi - \theta_c}{\pi \ell_c}\right), \tag{A8a}$$

$$u_r\big|_{Y=0} = -V_w, \tag{A8b}$$

where,

$$U_w = \frac{\mu U'_w}{\epsilon^2 \rho g \ell'^2_s}, \quad V_w = \frac{\mu V'_w}{\epsilon^3 \rho g \ell'^2_s}. \tag{A9}$$

In the absence of surface tension gradients and any externally imposed stresses, the tangential stress in the fluid vanishes at the free surface:

$$\left.\frac{\partial u_{\theta_c}}{\partial Y}\right|_{Y=H_c(\theta_c,t)} = 0, \tag{A10}$$

whereas the normal fluid stress undergoes a jump due to surface tension:

$$\begin{aligned} p\big|_{Y=H_c(\theta_c,t)} - p_a &= -\epsilon^2 \frac{\sigma}{\mu u'_c}\left\{1 + \epsilon\left(H_c + \frac{\partial^2 H_c}{\partial \theta_c^2}\right)\right\}, \\ &= -\frac{1}{\mathrm{Bo}}\left\{1 + \epsilon\left(H_c + \frac{\partial^2 H_c}{\partial \theta_c^2}\right)\right\}, \end{aligned} \tag{A11}$$

where p_a is the (uniform) air pressure in the cavity and σ is the surface tension of the air-fluid interface. In Eq. (A11), the term within {} is the (in-plane) film curvature at the angular position θ_c as a function of the film thickness H_c, and $\mathrm{Bo} = \rho g \ell'^2_s/\sigma$ is the Bond number, which is a dimensionless measure of the relative importance of gravity and surface tension in driving the film. Finally, we have the kinematic boundary condition, relating the (leading order) fluid velocity at the free surface to the rate of deformation of the film:

$$u_r\big|_{Y=H_c(\theta_c,t)} = -\frac{\partial H_c}{\partial t} - u_{\theta_c}\frac{\partial H_c}{\partial \theta_c}. \tag{A12}$$

One can solve Eq. (A7) subject to Eq. (A8a), and Eq. (A10) to obtain the following expression for the tangential fluid velocity:

$$u_{\theta_c}(\theta_c, Y, t) = \left(\frac{\partial p}{\partial \theta_c} - \sin\theta_c\right)\left(\frac{Y^2}{2} - Y H_c(\theta_c, t)\right) - U_w \tanh\left(\frac{\pi - \theta_c}{\pi \ell_c}\right), \tag{A13}$$

where the pressure gradient $\partial p/\partial\theta_{\rm c}$ can be calculated using Eqs. (A6) and (A11) as:

$$\frac{\partial p}{\partial\theta_{\rm c}} = -\frac{\epsilon}{\rm Bo}\frac{\partial}{\partial\theta_{\rm c}}\left(H_{\rm c} + \frac{\partial^2 H_{\rm c}}{\partial\theta_{\rm c}^2}\right). \tag{A14}$$

We can integrate Eq. (A2) from $Y = 0$ to $Y = H_{\rm c}(\theta_{\rm c}, t)$, and use Eqs. (A8b), (A12), (A13), and the Leibniz integration rule:

$$u_{\theta_{\rm c}}\frac{\partial H_{\rm c}}{\partial\theta_{\rm c}} + \int_0^{H_{\rm c}(\theta_{\rm c},t)}\frac{\partial u_{\theta_{\rm c}}}{\partial\theta_{\rm c}}\,dY = \frac{\partial}{\partial\theta_{\rm c}}\int_0^{H_{\rm c}(\theta_{\rm c},t)} u_{\theta_{\rm c}}(\theta_{\rm c}, Y, t)\,dY, \tag{A15}$$

to arrive at the final thin film equation for circular geometry given in the main text's Eq. (4),

$$\frac{\partial H_{\rm c}}{\partial t} + \frac{\partial Q_{\rm c}}{\partial\theta_{\rm c}} = V_{\rm w}, \tag{A16}$$

where,

$$\begin{aligned} Q_{\rm c}(\theta_{\rm c}, t) = \int_0^{H_{\rm c}(\theta_{\rm c},t)} u_{\theta_{\rm c}}(\theta_{\rm c}, Y, t)\,dY = \tfrac{H_{\rm c}^3}{3}\left[\tfrac{\epsilon}{\rm Bo}\tfrac{\partial}{\partial\theta_{\rm c}}\left(H_{\rm c} + \tfrac{\partial^2 H_{\rm c}}{\partial\theta_{\rm c}^2}\right) + \sin\theta_{\rm c}\right] \\ -U_{\rm w}\tanh\left(\tfrac{\pi-\theta_{\rm c}}{\pi\ell_{\rm c}}\right) H_{\rm c}(\theta_{\rm c}, t). \end{aligned} \tag{A17}$$

A.2 Description of the Numerical Method

We solve Eqs. (A16) and (A17) numerically using a semi-implicit finite-difference scheme. We first expand Eq. (A16) and write it as:

$$\begin{aligned} &\frac{\partial H_{\rm c}}{\partial t} + f_4^{\rm c}[H_{\rm c}, t]\frac{\partial^4 H_{\rm c}}{\partial\theta_{\rm c}^4} + f_3^{\rm c}[H_{\rm c}, t]\frac{\partial^3 H_{\rm c}}{\partial\theta_{\rm c}^3} + f_2^{\rm c}[H_{\rm c}, t]\frac{\partial^2 H_{\rm c}}{\partial\theta_{\rm c}^2} + f_1^{\rm c}[H_{\rm c}, t]\frac{\partial H_{\rm c}}{\partial\theta_{\rm c}} \\ &+ f_0^{\rm c}[H_{\rm c}, t]\,H_{\rm c}(\theta_{\rm c}, t) = V_{\rm w}, \end{aligned} \tag{A18}$$

where,

$$\begin{aligned} f_4^{\rm c}[H_{\rm c}, t] &= \frac{\epsilon}{\rm Bo}\frac{H_{\rm c}^3}{3}, \\ f_3^{\rm c}[H_{\rm c}, t] &= \frac{\epsilon}{\rm Bo}H_{\rm c}^2\frac{\partial H_{\rm c}}{\partial\theta_{\rm c}}, \\ f_2^{\rm c}[H_{\rm c}, t] &= \frac{\epsilon}{\rm Bo}\frac{H_{\rm c}^3}{3}, \\ f_1^{\rm c}[H_{\rm c}, t] &= H_{\rm c}^2\sin\theta_{\rm c} + \frac{\epsilon}{\rm Bo}H_{\rm c}^2\frac{\partial H_{\rm c}}{\partial\theta_{\rm c}} - U_{\rm w}\tanh\left(\frac{\pi-\theta_{\rm c}}{\pi\ell_{\rm c}}\right), \\ f_0^{\rm c}[H_{\rm c}, t] &= \frac{H_{\rm c}^2}{3}\cos\theta_{\rm c} - U_{\rm w}\frac{d}{d\theta_{\rm c}}\left\{\tanh\left(\frac{\pi-\theta_{\rm c}}{\pi\ell_{\rm c}}\right)\right\}. \end{aligned} \tag{A19}$$

Due to geometric symmetry (see Fig. 2a), Eq. (A18) is solved over the half-domain $0 \leq \theta_c \leq \pi$. We discretise Eq. (A18) in space (i.e. the θ_c derivatives) using second-order accurate finite difference approximations, and in time using an explicit Euler discretisation. The spatial discretisations are forward-and backward-biased at $\theta_c = 0$ and $\theta_c = \pi$, respectively. To obtain $H_c(\theta_c, t_{n+1})$, the functions $f_i[H_c, t]$ are evaluated at the (previous) time-step t_n, whereas the derivatives of H_c are evaluated at the desired/present time-step t_{n+1}. The numerical simulations are initialised by prescribing a uniform initial thickness $H_c(\theta_c, t = 0) = 0.1$.

A.3 Validation of the Numerical Method

We validate our numerical implementation in the limit $U_w = V_w = 0$, by comparing our results to existing solutions for the height of a thin film draining on the outer surface of a cylinder (McKinlay et al. 2023). We emphasise that this comparison can be made because the governing equation for our problem (where the film can be thought as developing inside a cylinder) is exactly the same as the problem where the film develops outside the cylinder. This is true even if gravity acts in opposite directions (with respect to the substrate normal extending into the fluid) depending on whether the film develops inside or outside the cylinder. The reason being, in the thin-film limit, the influence of gravity normal to the substrate is generally sub-dominant to leading order in $\epsilon = h'/\ell'_s$ (see Eqs. (A3), (A5) and (A6)) (Ashmore et al. 2003; Lopes et al. 2017). The time evolution of a thin film draining passively (under the influence of gravity) outside/inside a cylinder–for a specific Bond number–is shown in Fig. 11a, and the agreement between our results and those of McKinlay et al. (2023) validates our numerical method.

In addition to validating our numerical scheme in a limiting case, we confirm the resolution independence of the results provided in the main text. Towards this, we numerically solve Eq. (A18) for increasing resolutions N_θ (i.e. the number of discretised points at which the film height H_c is computed) and notice negligible change in the steady-state solution; some examples are provided in Fig. 11b.

Appendix B: 3D/Spherical System

B.1 Derivation of the Thin-Film Equation

For the spherical geometry, we work in spherical coordinates $\left(r', \theta_s, \phi\right)$. Since we are interested in an axisymmetric flow, the ϕ-component of the velocity and all derivatives with respect to the ϕ-coordinate are identically zero, i.e. $u'_\phi \equiv 0$ and $\partial(\,)/\partial\phi \equiv 0$. The derivation of the thin-film equation for the spherical geometry follows similar steps as that discussed for the circular case, and we provide here the main (dimensionless) equations required for deriving Eq. (7). The continuity equation is given by,

$$-\frac{\partial u_r}{\partial Z} + \frac{1}{\sin\theta_s}\frac{\partial}{\partial\theta_s}\left(u_{\theta_s}\sin\theta_s\right) = 0, \tag{B20}$$

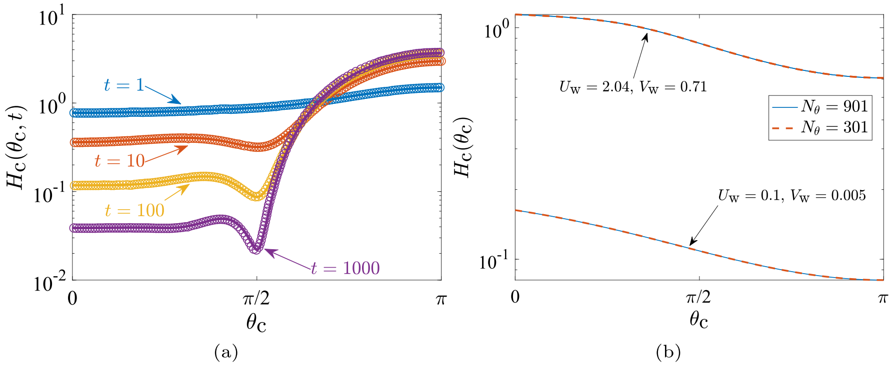

Fig. 11 **a** Comparison between the finite-difference solution in the 2D case, Eq. (A16) (with $U_w = V_w = 0$) in the present work and the numerical solution of McKinlay et al. (2023) (see their Fig. 2) for the drainage of a thin film over a circular cylinder, at dimensionless times $t = 1, 10, 100, 1000$. The symbols denote numerical solutions of McKinlay et al. (2023) and the solid lines denote our solutions. The Bond number for these film profiles is such that $\epsilon/\text{Bo} = (\pi^2 - 8)/(8\pi) \approx 0.07439$. **b** Convergence of the numerical solution to Eq. (A18) for different numbers of grid points N_θ, shown for two different values of (U_w, V_w)

the r'-momentum equation is,

$$\frac{\partial p}{\partial Z} = \epsilon \cos\theta_s \sim O(\epsilon) \approx 0, \tag{B21}$$

where Z, just like Y in the circular case, is a local stretched coordinate normal to the walls of the spherical cavity, such that $Z = 0$ denotes the cavity walls and $Z = H_s$ denotes the free surface of the fluid (Fig. 10b). The θ_s-momentum equation is given by,

$$-\frac{\partial p}{\partial \theta_s} + \frac{\partial^2 u_{\theta_s}}{\partial Z^2} + \sin\theta_s = 0. \tag{B22}$$

The boundary conditions for the velocities $\left(u_{\theta_s}, u_r\right)$ at $Z = 0$ are, just as in the circular case:

$$u_{\theta_s}\big|_{Z=0} = -U_w \tanh\left(\frac{\pi - \theta_s}{\pi \ell_c}\right), \tag{B23a}$$

$$u_r\big|_{Z=0} = -V_w, \tag{B23b}$$

where, (U_w, V_w) were defined before in Eq. (A9).

The tangential stress boundary condition is:

$$\left.\frac{\partial u_{\theta_s}}{\partial Z}\right|_{Z=H_s(\theta_s,t)} = 0, \tag{B24}$$

whereas the normal fluid stress condition is:

$$p\big|_{Z=H_s(\theta_s,t)} - p_a = -\frac{1}{\mathrm{Bo}}\left\{2+\epsilon\left(2H_s + \frac{\partial H_s}{\partial \theta_s}\cot\theta_s + \frac{\partial^2 H_s}{\partial \theta_s^2}\right)\right\}, \tag{B25}$$

where, again, the term within {} is the film curvature at the angular position θ_s as a function of the film thickness H_s. We also have the kinematic boundary condition as:

$$u_r\big|_{Z=H_s(\theta_s,t)} = -\frac{\partial H_s}{\partial t} - u_{\theta_s}\frac{\partial H_s}{\partial \theta_s}. \tag{B26}$$

Following exactly the same steps as in the circular case, we obtain the following expression for the fluid velocity,

$$u_{\theta_s}(\theta_s, Z, t) = \left(\frac{\partial p}{\partial \theta_s} - \sin\theta_s\right)\left(\frac{Z^2}{2} - ZH_s(\theta_s,t)\right) - U_w \tanh\left(\frac{\pi-\theta_s}{\pi\ell_c}\right) \tag{B27}$$

where, now the pressure gradient is derived from Eq. (B25) as,

$$\frac{\partial p}{\partial \theta_s} = -\frac{\epsilon}{\mathrm{Bo}}\frac{\partial}{\partial \theta_s}\left(2H_s + \frac{\partial H_s}{\partial \theta_s}\cot\theta_s + \frac{\partial^2 H_s}{\partial \theta_s^2}\right). \tag{B28}$$

Integrating Eq. (B20) from $Z = 0$ to $Z = H_s(\theta_s, t)$, and using Eqs. (B23b), (B26), (B27), and the Leibniz integration rule:

$$u_{\theta_s}\sin\theta_s\frac{\partial H_s}{\partial \theta_s} + \int_0^{H_s(\theta_s,t)} \frac{\partial}{\partial \theta_s}\left(u_{\theta_s}\sin\theta_s\right) dZ = \frac{\partial}{\partial \theta_s}\int_0^{H_s(\theta_s,t)} u_{\theta_s}(\theta_s, Z)\sin\theta_s\, dZ, \tag{B29}$$

we obtain the final thin film equation for spherical geometry given in the main text,

$$\frac{\partial H_s}{\partial t} + \frac{1}{\sin\theta_s}\frac{\partial Q_s}{\partial \theta_s} = V_w, \tag{B30}$$

where,

$$\begin{aligned} Q_s(\theta_s,t) = {} & \frac{H_s^3\sin\theta_s}{3}\left[\frac{\epsilon}{\mathrm{Bo}}\frac{\partial}{\partial \theta_s}\left(2H_s + \frac{\partial H_s}{\partial \theta_s}\cot\theta_s + \frac{\partial^2 H_s}{\partial \theta_s^2}\right) + \sin\theta_s\right] \\ & - U_w\sin\theta_s\tanh\left(\frac{\pi-\theta_s}{\pi\ell_c}\right)H_s(\theta_s,t). \end{aligned} \tag{B31}$$

B.2 Details of the Numerical Method

The numerical method is identical to that used for circular geometry, except that the domain extends from $0 < \theta_e \le \theta_s \le \pi$ (see Fig. 2b). We do not repeat the details of

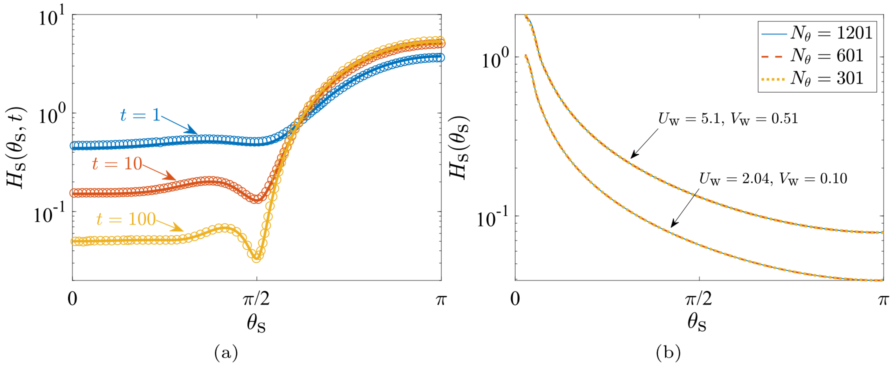

Fig. 12 Comparison between the finite-difference 3D solution to Eq. (B30) (with $U_\mathrm{w} = V_\mathrm{w} = 0$, $\theta_\mathrm{e} = 0$) in the present work and the numerical solution of Qin et al. (2020) (see their Fig. 2) for the drainage of a thin film over a sphere, at dimensionless times $t = 1, 10, 100$. The symbols denote numerical solutions of Qin et al. (2020) and the solid lines denote our solutions. The Bond number for these film profiles is such that $\epsilon/\mathrm{Bo} = 1/24$. **b** Convergence of the numerical solution to Eq. (B32) for different numbers of discretization grid points N_θ, shown for two different values of $(U_\mathrm{w}, V_\mathrm{w})$

the numerical method and provide here just the expanded form of Eq. (B30):

$$\frac{\partial H_\mathrm{s}}{\partial t} + f_4^\mathrm{s}[H_\mathrm{s}, t]\frac{\partial^4 H_\mathrm{s}}{\partial \theta_\mathrm{s}^4} + f_3^\mathrm{s}[H_\mathrm{s}, t]\frac{\partial^3 H_\mathrm{s}}{\partial \theta_\mathrm{s}^3} + f_2^\mathrm{s}[H_\mathrm{s}, t]\frac{\partial^2 H_\mathrm{s}}{\partial \theta_\mathrm{s}^2} + f_1^\mathrm{s}[H_\mathrm{s}, t]\frac{\partial H_\mathrm{s}}{\partial \theta_\mathrm{s}}$$
$$+ f_0^\mathrm{s}[H_\mathrm{s}, t]\, H_\mathrm{s}(\theta_\mathrm{s}, t) = V_\mathrm{w}, \tag{B32}$$

where,

$$\begin{aligned}
f_4^\mathrm{s}[H_\mathrm{s}, t] &= \frac{\epsilon}{\mathrm{Bo}}\frac{H_\mathrm{s}^3}{3},\\
f_3^\mathrm{s}[H_\mathrm{s}, t] &= \frac{\epsilon}{\mathrm{Bo}}\left(\frac{2H_\mathrm{s}^3}{3}\cot\theta_\mathrm{s} + H_\mathrm{s}^2\frac{\partial H_\mathrm{s}}{\partial \theta_\mathrm{s}}\right),\\
f_2^\mathrm{s}[H_\mathrm{s}, t] &= \frac{\epsilon}{\mathrm{Bo}}\left(-\frac{H_\mathrm{s}^3}{3}\cot^2\theta_\mathrm{s} + H_\mathrm{s}^2\cot\theta_\mathrm{s}\frac{\partial H_\mathrm{s}}{\partial \theta_\mathrm{s}}\right),\\
f_1^\mathrm{s}[H_\mathrm{s}, t] &= H_\mathrm{s}^2\sin\theta_\mathrm{s} + \frac{\epsilon}{\mathrm{Bo}}\left\{H_\mathrm{s}^3\left(\frac{\cot^3\theta_\mathrm{s}}{3} + \cot\theta_\mathrm{s}\right) - H_\mathrm{s}^2\frac{\cos 2\theta_\mathrm{s}}{\sin^2\theta_\mathrm{s}}\frac{\partial H_\mathrm{s}}{\partial \theta_\mathrm{s}}\right\}\\
&\quad - U_\mathrm{w}\tanh\left(\frac{\pi - \theta_\mathrm{s}}{\pi \ell_\mathrm{c}}\right),\\
f_0^\mathrm{s}[H_\mathrm{s}, t] &= \frac{2H_\mathrm{s}^2}{3}\cos\theta_\mathrm{s} - U_\mathrm{w}\tanh\left(\frac{\pi - \theta_\mathrm{s}}{\pi \ell_\mathrm{c}}\right)\cot\theta_\mathrm{s} - U_\mathrm{w}\frac{d}{d\theta_\mathrm{s}}\left\{\tanh\left(\frac{\pi - \theta_\mathrm{s}}{\pi \ell_\mathrm{c}}\right)\right\}.
\end{aligned} \tag{B33}$$

B.3 Validation of the Numerical Method

We validate our numerical solution in the limit $U_\mathrm{w} = V_\mathrm{w} = 0$ and $\theta_\mathrm{e} = 0$, by comparing our solution to existing results for the height of a thin film draining on the outer surface of a sphere (Qin et al. 2020). As in the 2D case, it is important to note that this comparison is possible because, in the thin-film limit, the governing equation for our problem (where the film develops inside a sphere) is the same as the problem where the film develops outside the sphere. The comparison–for a prescribed Bond number–is shown in Fig. 12a, and the agreement between our results and those of Qin et al. (2020) validates our numerical method. The convergence of the solution to Eq. (B32) with respect to the resolution of spatial discretization (i.e. the number of points N_θ at which H_s is computed), is shown in Fig. 12b.

Acknowledgements We thank Bartlomiej Waclaw for useful comments. This work was funded by EPSRC (grant EP/W024012/1 to EL).

Data availability The results in this manuscript are based on theoretical derivations and not on existing experimental data. All steps of the derivations are given in the manuscript's Appendix and thus can be used/reproduced as such.

References

Albers GM, Tomkiewicz RP, May MK, Ramirez OE, Rubin BK (1996) Ring distraction technique for measuring surface tension of sputum: relationship to sputum clearability. J Appl Physiol 81(6):2690–2695. https://doi.org/10.1152/jappl.1996.81.6.2690

Ashmore J, Hosoi AE, Stone HA (2003) The effect of surface tension on rimming flows in a partially filled rotating cylinder. J Fluid Mech 479:65–98. https://doi.org/10.1017/s0022112002003312

Beule AG (2010) Physiology and pathophysiology of respiratory mucosa of the nose and the paranasal sinuses. GMS Current Topics in Otorhinolaryngology - Head and Neck Surgery; 9:Doc07; ISSN 1865-1011 https://doi.org/10.3205/CTO000071

Blanton PL, Biggs NL (1969) Eighteen hundred years of controversy: the paranasal sinuses. Am J Anat 124(2):135–147. https://doi.org/10.1002/aja.1001240202

Bluestone CD, Pagano AS, Swarts JD, Laitman JT (2012) Consequences of evolution: is rhinosinusitis, like otitis media, a unique disease of humans? Otolaryngol Head Neck Surg 147(6):986–991. https://doi.org/10.1177/0194599812461892

Bull JL, Nelson LK, Walsh JT, Glucksberg MR, Schürch S, Grotberg JB (1999) Surfactant-spreading and surface-compression disturbance on a thin viscous film. J Biomech Eng 121(1):89–98. https://doi.org/10.1115/1.2798049

Butaric LN, Wadle M, Gascon J (2018) Anatomical variation in maxillary sinus ostium positioning: implications for nasal-sinus disease. Anat Rec 302(6):917–930. https://doi.org/10.1002/ar.24039

Button B, Cai L, Ehre C, Kesimer M, Hill DB, Sheehan JK, Boucher RC, Rubinstein M (2012) A periciliary brush promotes the lung health by separating the mucus layer from airway epithelia. Science 337(6097):937–941. https://doi.org/10.1126/science.1223012

Chen Z, Zhong M, Luo Y, Deng L, Hu Z, Song Y (2019) Determination of rheology and surface tension of airway surface liquid: a review of clinical relevance and measurement techniques. Respir Res. https://doi.org/10.1186/s12931-019-1229-1

Cho SH, Kim TH, Kim KR, Lee J, Lee D, Kim J, Im J, Park C, Hwang K (2010) Factors for maxillary sinus volume and craniofacial anatomical features in adults with chronic rhinosinusitis. Arch Otolaryngol-Head Neck Surg 136(6):610–615. https://doi.org/10.1001/archoto.2010.75

Cohen NA (2006) Sinonasal mucociliary clearance in health and disease. Annal Otol, Rhinol Laryngol 115(9–suppl):20–26. https://doi.org/10.1177/00034894061150S904

Craster RV, Matar OK (2000) Surfactant transport on mucus films. J Fluid Mech 425:235–258. https://doi.org/10.1017/s0022112000002317

Craster RV, Matar OK (2009) Dynamics and stability of thin liquid films. Rev Mod Phys 81(3):1131–1198. https://doi.org/10.1103/revmodphys.81.1131

Drettner B (1980) Pathophysiology of paranasal sinuses with clinical implications. Clin Otolaryngol Allied Sci 5(4):277–284. https://doi.org/10.1111/j.1365-2273.1980.tb02145.x

Fahy JV, Dickey BF (2010) Airway mucus function and dysfunction. N Engl J Med 363(23):2233–2247. https://doi.org/10.1056/nejmra0910061

Fokkens WJ, Lund VJ, Hopkins C, Hellings PW, Kern R, Reitsma S, Toppila-Salmi S, Bernal-Sprekelsen M, Mullol J (2020) Executive summary of epos 2020 including integrated care pathways. Rhinol J 58(2):82–111. https://doi.org/10.4193/rhin20.601

Gizurarson S (2015) The effect of cilia and the mucociliary clearance on successful drug delivery. Biol Pharm Bull 38(4):497–506. https://doi.org/10.1248/bpb.b14-00398

Hamed R, Fiegel J (2013) Synthetic tracheal mucus with native rheological and surface tension properties. J Biomed Mater Res, Part A 102(6):1788–1798. https://doi.org/10.1002/jbm.a.34851

Hill DB, Button B, Rubinstein M, Boucher RC (2022) Physiology and pathophysiology of human airway mucus. Physiol Rev 102(4):1757–1836. https://doi.org/10.1152/physrev.00004.2021

Jones N (2001) The nose and paranasal sinuses physiology and anatomy. Adv Drug Deliv Rev 51(1–3):5–19. https://doi.org/10.1016/s0169-409x(01)00172-7

Kaliner M, Marom Z, Patow C, Shelhamer J (1984) Human respiratory mucus. J Allergy Clin Immunol 73(3):318–323. https://doi.org/10.1016/0091-6749(84)90403-2

Kang D, Nadim A, Chugunova M (2016) Dynamics and equilibria of thin viscous coating films on a rotating sphere. J Fluid Mech 791:495–518. https://doi.org/10.1017/jfm.2016.67

Keir J (2008) Why do we have paranasal sinuses? J Laryngol Otol 123(1):4–8. https://doi.org/10.1017/s0022215108003976

Kim S, Ward LA, Butaric LN, Maddux SD (2021) Ancestry-based variation in maxillary sinus anatomy: implications for health disparities in sinonasal disease. Anat Rec 305(1):18–36. https://doi.org/10.1002/ar.24644

Kirihene RK, Rees G, Wormald P (2002) The influence of the size of the maxillary sinus ostium on the nasal and sinus nitric oxide levels. Am J Rhinol 16(5):261–264. https://doi.org/10.1177/194589240201600508

Knowles MR, Boucher RC (2002) Mucus clearance as a primary innate defense mechanism for mammalian airways. J Clin Investig 109(5):571–577. https://doi.org/10.1172/jci0215217

Lai SK, Wang Y, Wirtz D, Hanes J (2009) Micro- and macro-rheology of mucus. Adv Drug Deliv Rev 61(2):86–100. https://doi.org/10.1016/j.addr.2008.09.012

Leal LG (2007) Advanced transport phenomena: fluid mechanics and convective transport processes. Cambridge University Press, Cambridge

Lopes AB, Thiele U, Hazel AL (2017) On the multiple solutions of coating and rimming flows on rotating cylinders. J Fluid Mech 835:540–574. https://doi.org/10.1017/jfm.2017.756

Lund VJ (1996) Nasal physiology: neurochemical receptors, nasal cycle, and ciliary action. In: Allergy and Asthma Proceedings, vol. 17, p. 179. OceanSide Publications

McKinlay RA, Wray AW, Wilson SK (2023) Late-time draining of a thin liquid film on the outer surface of a circular cylinder. Phys Rev Fluids. https://doi.org/10.1103/physrevfluids.8.084001

McShane A, Bath J, Jaramillo AM, Ridley C, Walsh AA, Evans CM, Thornton DJ, Ribbeck K (2021) Mucus. Curr Biol 31(15):938–945. https://doi.org/10.1016/j.cub.2021.06.093

Olivença DV, Fonseca LL, Voit EO, Pinto FR (2019) Thickness of the airway surface liquid layer in the lung is affected in cystic fibrosis by compromised synergistic regulation of the enac ion channel. J R Soc Interface 16(157):20190187. https://doi.org/10.1098/rsif.2019.0187

Oron A, Davis SH, Bankoff SG (1997) Long-scale evolution of thin liquid films. Rev Mod Phys 69(3):931–980. https://doi.org/10.1103/revmodphys.69.931
Papadopoulou A, Chrysikos D, Samolis A, Tsakotos G, Troupis T (2021) Anatomical variations of the nasal cavities and paranasal sinuses: a systematic review. Cureus 13(1):e12727. https://doi.org/10.7759/cureus.12727
Patne R (2024) Effect of inhaled air temperature on mucus dynamics in the proximal airways. J Fluid Mech. https://doi.org/10.1017/jfm.2023.1030
PDQ Adult Treatment Editorial Board: Paranasal Sinus and Nasal Cavity Cancer Treatment (Adult) (PDQ ®): Patient Version, https://www.ncbi.nlm.nih.gov/books/NBK66003/ PMID:26389439 (2002)
Proctor DF, Andersen I (1982) The Nose: Upper Airway Physiology and the Atmospheric Environment. Elsevier Biomedical Press, Amsterdam
Qin J, Xia Y, Gao P (2020) Axisymmetric evolution of gravity-driven thin films on a small sphere. J Fluid Mech. https://doi.org/10.1017/jfm.2020.816
Sanderson MJ, Sleigh MA (1981) Ciliary activity of cultured rabbit tracheal epithelium: beat pattern and metachrony. J Cell Sci 47(1):331–347. https://doi.org/10.1242/jcs.47.1.331
Satir P, Sleigh MA (1990) The physiology of cilia and mucociliary interactions. Annu Rev Physiol 52(1):137–155. https://doi.org/10.1146/annurev.ph.52.030190.001033
Silberberg A (1983) Biorheological matching: mucociliary interaction and epithelial clearance. Biorheology 20(2):215–222. https://doi.org/10.3233/bir-1983-20211
Smith DJ, Gaffney EA, Blake JR (2008) Modelling mucociliary clearance. Respir Physiol Neurobiol 163(1–3):178–188. https://doi.org/10.1016/j.resp.2008.03.006
Stevens WW, Lee RJ, Schleimer RP, Cohen NA (2015) Chronic rhinosinusitis pathogenesis. J Allergy Clin Immunol 136(6):1442–1453. https://doi.org/10.1016/j.jaci.2015.10.009
Whyte A, Boeddinghaus R (2019) The maxillary sinus: physiology, development and imaging anatomy. Dentomaxillofacial Radiol 48(8):20190205. https://doi.org/10.1259/dmfr.20190205
Winslow T © (2012) Terese Winslow LLC, U.S. Govt. has certain rights
Yalcin ED, Koparal M, Aksoy O (2018) The effect of ectodermal dysplasia on volume and surface area of maxillary sinus. Eur Arch Otorhinolaryngol 275(12):2991–2996. https://doi.org/10.1007/s00405-018-5177-z